Workshop of
Experimental Nuclear and Particle Physics
2021

30th April – 23rd June 2021, Prague

Faculty of Nuclear Sciences and Physical Engineering
Czech Technical University in Prague

Workshop of Experimental Nuclear and Particle Physics 2021

Editors:	L. Novotný
Issued by:	Czech Technical University in Prague
	Faculty of Nuclear Sciences and Physical Engineering
Address:	KF FJFI ČVUT, Břehová 7, 115 19 Praha 1
	novotl23@fjfi.cvut.cz, +420728222668

Available at https://indico.fjfi.cvut.cz/event/185/attachments/1090/1539/WEJCF2021_sbornik.pdf
First edition. 45 pages.

Contents

Foreword

This year, for the 15$^{\mathrm{th}}$ time, students, graduates, and teachers from the field of Experimental Nuclear and Particle Physics at FNSPE CTU met at the annual winter workshop. Due to the pandemic situation, the meeting was held during two months (30th April - 23rd June 2021) in online version using ZOOM interface. The closing banquet was held in Vila Lanna, Prague. The main goal of the workshop is to follow the progress of students, discuss problems and experiences and also to get to know each other better. Each participant gave a talk about their work or progress during the previous year. Extended abstracts of these talks are published in the document you are holding now.

Editors

Electrons from open heavy-flavor hadron decays in heavy-ion collisions at STAR

Carolina S. Lopes

1 Introduction

In relativistic heavy-ion collisions at RHIC and LHC energies, a hot and dense medium of deconfined and strongly interacting matter - the Quark-Gluon Plasma (QGP) - is formed. Important probes of the QGP include heavy (charm and bottom) quarks [1, 2], which are produced early in the collisions and expected to not fully thermalize [3]. The most feasible way to study heavy quarks is via electrons from semileptonic decays (Heavy Flavor Electrons - HFE).

The main purpose of this research project is to study the HFE energy loss in the medium formed in Au-Au collisions with a center-of-mass energy $\sqrt{s_{NN}}$ of 54 GeV at the STAR Experiment at RHIC. By extracting the nuclear modification factor R_{AA} of the HFE yields, one can compare the obtained results with different collision energies. To calculate R_{AA}, some steps need to be accomplished beforehand.

First, it is necessary to identify the nonphotonic electrons (NPE) out of our inclusive electron (INCL) sample, by subtracting the photonic electrons (PE) contribution [4]. This is better illustrated in equation 1, which also considers the purity of the inclusive electrons and the efficiency of the photonic electrons reconstruction. Once the nonphotonic electrons are identified, we can exclude the electrons from hadron decays to finally obtain the heavy flavor electron yield.

$$N_{NPE} = \frac{N_{incl} \cdot \epsilon_{purity} - \frac{N_{PE}}{\epsilon_{PE}}}{\epsilon_{NPE}} \tag{1}$$

Another important step within this project is to include information of the Barrel Electromagnetic Calorimeter in order to assist in the inclusive electron identification. This information is newly available for the analyzed data sample, and needs to be carefully interpreted.

2 The STAR Experiment

The STAR (Solenoidal Tracker At RHIC) detector system was constructed with the main goal of finding QGP signatures in heavy-ion collisions, and of studying the behavior of strongly interacting matter [5]. STAR has a large acceptance both in pseudorapidity ($0 < |\eta| < 1$) and azimuth ($0 < \phi < 2\pi$), thus favoring the event-by-event characterization of the collisions. For this analysis, four of the STAR subdetector systems will be used:

- The Vertex Position Detector (VPD) is employed for minimum bias triggering.
- The Time Projection Chamber (TPC), a gas chamber built for momentum measurement, is used to identify charged particles via energy loss measurements.
- The Time of Flight (TOF), which uses both information of the VPD and of its resistive plate chambers to calculate the time of flight of the particles incoming from the collision.

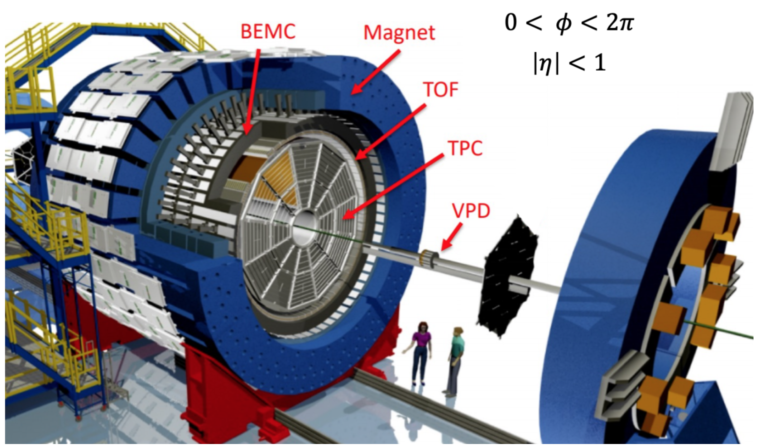

Figure 1: Scheme of the STAR detector with its subsystems. Adapted from [6].

- The Barrel Electromagnetic Calorimeter (BEMC), which measures the deposited energy of particles, being important to distinguish electrons from hadrons at intermediate to high pT. The BEMC consists of 120 modules of 40 towers, which point to the interaction region.

A scheme of STAR and its detector subsystems, highlighting the aforementioned detectors, is shown in Figure 1.

3 Data Analysis

The analyzed data sample refers to mid-central collisions (0-60% centrality), and comprises ca. 1E9 events before track selection and ca. 5.8E8 events after track selection. BEMC information is included to improve the electron identification, in addition to the TOF and TPC cuts ($1/\beta$ and nSigma, respectively).

The BEMC electron identification is carried out based on the energy that the electrons deposit in the calorimeter when encountering it. Electrons are expected to deposit approximately all their energy in the BEMC towers and produce electromagnetic showers. It may happen that an electron shower spreads out of a single tower. In these cases, one can consider the cluster energy instead of the tower energy. A cluster corresponds to the set of the tower with the maximum energy, together with its neighboring towers.

The energy to momentum ratio (E/p) of the electrons lies around 1, as they travel with velocity near to the speed of light. By selecting a good the E/p interval of interest, one can then identify electrons with a low hadron contamination and a good efficiency at medium to high transverse momentum (pT > 1.5 GeV/c). In this study, we compare the E/p spectra for both cluster and tower energy to identify where to best cut on the energy.

Another important step when including BEMC information is to check whether there are towers which fired more often then the average - hot towers - during certain runs. Hot towers may alter the E/p spectra if triggered data is to be analyzed in the future, and shall then be excluded from our study. In this study, we check which towers have this characteristic during 614 different runs.

4 Conclusions and Outlook

The results of the previous steps were presented in the EJČF seminar on 07.05.2021. Adding the BEMC information in the analysis code, studying the E/p spectra and marking the BEMC hot towers constitute crucial steps to the future calculation of the HFE yields, and consequently of R_{AA}.

References

[1] L Adamczyk, J Kevin Adkins, G Agakishiev, MM Aggarwal, Z Ahammed, NN Ajitanand, I Alekseev, DM Anderson, R Aoyama, A Aparin, et al. Elliptic flow of electrons from heavy-flavor hadron decays in Au+Au collisions at $\sqrt{s_{NN}} = 200$, 62.4, and 39 GeV. *Physical Review C*, 95(3):034907, 2017.

[2] Xin Dong and Vincenzo Greco. Heavy quark production and properties of quark-gluon plasma. *Progress in Particle and Nuclear Physics*, 104:97–141, 2019.

[3] Xin Dong, Yen-Jie Lee, and Ralf Rapp. Open heavy-flavor production in heavy-ion collisions. *Annual Review of Nuclear and Particle Science*, 69:417–445, 2019.

[4] Mustafa Mustafa. Experimental study of electrons from heavy flavor hadrons decays in Au+Au collisions at 200, 62.4 and 39 GeV in the STAR experiment at RHIC. *PhD. Thesis. Purdue University*, 2013.

[5] KH Ackermann, N Adams, C Adler, Z Ahammed, S Ahmad, C Allgower, J Amonett, J Amsbaugh, BD Anderson, M Anderson, et al. STAR detector overview. *Nuclear Instruments and Methods in Physics Research Section A: Accelerators, Spectrometers, Detectors and Associated Equipment*, 499(2-3):624–632, 2003.

[6] Yi Yang. The STAR detector upgrades for the BES-II and beyond physics program. In *Quark Matter 2019*, 2019.

MEASUREMENT OF ELECTRON BUNCH DURATION IN LASER-DRIVEN PLASMA-BASED ACCELERATORS

Patrik Puškáš

1 Introduction

My bachelor's thesis focuses on laser driven plasma based accelerators. At first I want to describe basic principles behind the generation of high intensity laser pulses and plasma physics. Then my thesis focuses on methods of electron acceleration in plasma using high intensity laser pulses. I focused especially on the most common acceleration method called Laser WakeField Acceleration or LWFA for short. After that I describe currently used methods for measurement of electron bunch duration. The final chapter is devoted to developping a diagnostic for ultra-short electron bunch duration from LWFA.

2 Laser Wakefield acceleration

Laser Wakefield acceleration is relatively new concept developed in 1972 [1]. During LWFA the acceleration gradient is much higher than in conventional accelerators. These higher gradients (in hundreds GV/m) then allow the use of shorter acceleration distances (in centimeters) and consequently the accelerators can be build much shorter. LWFA operates on a principle of high-energy laser pulse, which propagates through plasma and it pushes electron from its path, their respective ions stand relatively stationary. This creates a charge separation in a wake of this laser pulse, when electrons are trying to move to their original place. This creates charge oscillations and plasma waves. These waves then function as acceleration cavities for electrons.

The development of LWFA was made possible by advancements in generation of high-energy laser pulses, most notably Chirped Pulse Amplification, or CPA for short. This method, develloped by Donna Strickland and Gerard Morou in 1985 [2] which allowed to amplify an ultra-short laser pulse up to the petawatt levels, is critical for producing high-energy laser pulses that have enough energy to produce desired plasma waves. First demostration of LWFA was made in 1994 [1]. The next steps in development was the invention of so called "bubble regime" in 2004 [3]. Today, we are able to produce the energy gradients in several GeV per few centimeters [4]. The development of this acceleration method is still ongoing and part of a current research.

3 Few femtoseconds electron bunch produced by a laser-plasma accelerator

LWFA method of electron acceleration produces ultra-short electron bunches, meaning accelerating electric fields of several hundreds gigavolts per metre and deliver high quality electron beams with low energy spread up to 1 GeV peak energy [5]. The expected duration of electron bunch from our models is $\tau \approx 10$ fs [6]. However, the commonly used methods for measuring electron bunch duration, such as streak cameras or radio-frequency sweeping cavities do not have the temporal resolution required for femtosecond bunches [7]. However, we can use coherent transition radion, or CTR that is emitted by the electron bunch as it passes through a thin metallic foil. The possible experimental setup is shown in Fig. 2. We can analyse the spectrum of produced radiation and then compare it to our predicted spectrum for different temporal duration σ, as seen in Fig. 3 [7].

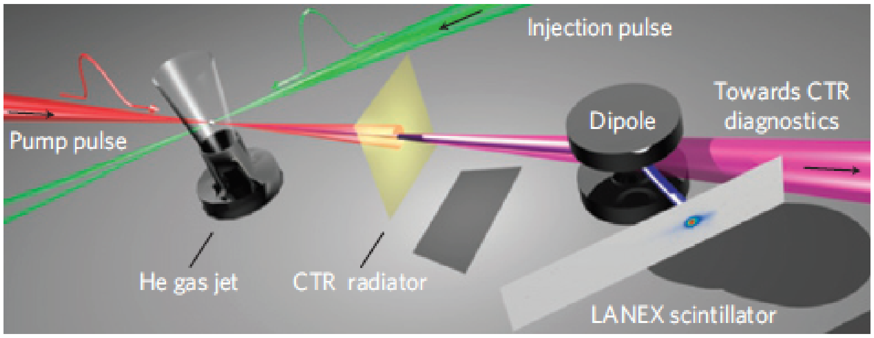

Figure 2: Possible experimental arrangement. The accelerated electron beam (blue) traverses an aluminium foil and generates transition radiation in a narrow cone along the forward direction, represented by violet color. The electron beam is then diverted and analysed for calculations. The transition radiation exits the interaction chamber for later characterization. From [7].

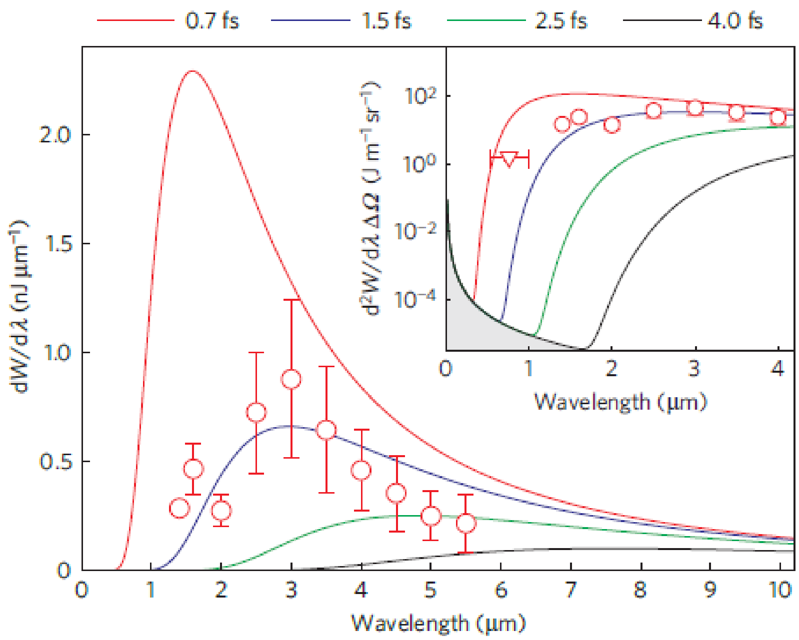

Figure 3: The comparison between predicted spectrum shape with the experimental data. The analytical CTR spectra for different bunch durations are represented by solid lines. The bunch shape is taken to be Gaussian with r.m.s. duration σ, as indicated by the legend. Experimental spectrum was taken by infrared monochromator (circles) and the visible spectrometer (triangles). Error bars indicate shot fluctuations and spectral range of the measurement. From [7].

However, from this CTR spectrum we can now only deduce the temporal distribution of one electron bunch. We cannot determine the spatial distribution of the electrons. There are several options possible configurations in which electrons can be arranged in one electron bunch, from normal to random distribution. We also have to determine, if the consequent electron bunches have more/less or the same number of charge carriers as the previous bunch. The main focus of my bachelor thesis is to predict the spectrum for several cases of spatial distribution, compare them and propose a possible diagnostic to measure the differences between them.

References

[1] Tajima, T. and Dawson, J. M. Laser Electron Accelerator. In *Phys. Rev. Let. 43*, pages 267–270. 1979.

[2] Strickland, D. and Mourou, G. Compression of ampli
ed chirped optical pulses. In *Optics Communications 55.6*, pages 447–449. 1985.

[3] Pukhov, A. and Meyer-ter Vehn, J. Laser wakefi
eld acceleration: the highly non-linear broken-wave regime. In *Applied Physics B 74.4*, pages 355–361. 2002.

[4] Wiggins, S. M. and Isaac, R. C. et al. High Quality Electron Beams from a Laser Wakefi
eld Accelerator. In *Conference on Lasers and Electro-Optics 2010. Optical Society of America,*, 2010.

[5] Leemans, W. P. et al. GeV Electron beams from a centimetre-scale accelerator. In *Nature Phys. 2*, pages 696–699. 2006

[6] Faure, J. et al. A laser-plasma accelerator producing monoenergetic electron beams. In *Nature 431*, pages 541–544. 2004.

[7] George Kour and Raid Saabne. Few femtosecond, few kiloampere electron bunch produced by a laser–plasma accelerator. In *Nature Physics volume 7*, pages 219–222. 2011.

Characterisation of plasma waves generated by intense laser pulses

David Gregocki

Abstract

The first publication that suggested that electrons can be accelerated by a plasma wave created by an intense laser pulse was the now-famous article entitled “Laser Electron Accelerator” by Tajima and Dawson published in 1979 [1]. At that time, many scientists studied properties of intense laser pulses, especially their ability to generate extremely high energy densities, which unveiled the potential for creating a particle accelerator with very high field gradients and thus compact, and very efficient acceleration. A fundamental tenet of laser-driven plasma-based electron acceleration is that the plasma in the laser accelerator acts as an energy transformer, where energy is transferred from the driver, for example an ultra-short, ultra-intense pulsed laser, to accelerated particles. With this approach, a plasma acceleration with an acceleration gradient of 1 GeV/cm can be achieved. Several methods of laser-driven plasma-based electron acceleration, which differ from the type or properties of the driver, can be described, namely plasma wakefield acceleration, plasma beat wave acceleration, acceleration by a train of short laser pulses, self-modulated laser wakefield acceleration, and others [2]. A method predominantly studied here is called laser wakefield acceleration (LWFA). In this technique, an ultra-short, high intensity laser pulse propagates through underdense plasma or gas, which is immediately ionized by the laser pulse itself. This inhomogeneous electromagnetic radiation results in the so-called ponderomotive force, which expels the electrons from assumingly stationary ions (due to their mass) from its path in the radial and axial directions. As a result, areas with higher and lower electron density are created, together with an electric field with a phase velocity approximately equal to the speed of light. However, the expelled electrons are attracted back to the ions via Coulomb forces and subsequently repelled again due to the ponderomotive force. These density modulations lead to the formation of the plasma wakefield [1]. The phase velocity of the plasma wave corresponds to the group velocity of the laser pulse. Background electrons, under appropriate conditions, can also be injected into a plasma wave and be accelerated to ultrarelativistic energies. Methods for injecting and trapping plasma electrons in plasma waves are also discussed. In general, LWFA can operate in one of two regimes, and that is the quasilinear or nonlinear bubble regime. At a sufficiently high intensity of the driver pulse ($a_0 \gg 1$) with a length $L < \lambda_p/2$, all plasma electrons are expelled from the region around the pulse propagation axis. As a result, bubbles are formed instead of mentioned plasma waves. Because the driver pulse leaves such bubbles behind, this regime is known as a bubble (or blow-out) regime (see Figure19). Moreover, due to the fact that bubble regime operates with a higher acceleration gradients, due to the stronger electron density modulation, the structure of the created electric fields in the plasma bubbles are more suitable for electron acceleration. Evolution of plasma wake structures is a key element of the function of laser-driven plasma wakefield accelerators. However, detailed knowledge of such evolution is currently most available from intensive computer simulations. In the last three decades, many diagnostic methods of the plasma wakefield have been studied and developed, such as: frequency domain interferometry (FDI), photon acceleration diagnostic (PAD), frequency domain holography (FDH), frequency domain shadowgraphy (FDS), and others. For example, frequency-domain interferometry (FDI) applies an ultra-short probe pulse pair one before and one after a driver laser pulse. The measurement of the phase difference between the those two probe pulses, which originated from the created plasma density oscillation, delivers the local electron density at only a single time delay behind the driving pulse. The wake structure is determined by a long multi-shot measurement averaging over shot-to-shot variations of the laser-generated plasma structure. However, as FDI method neglects the influence of the probe

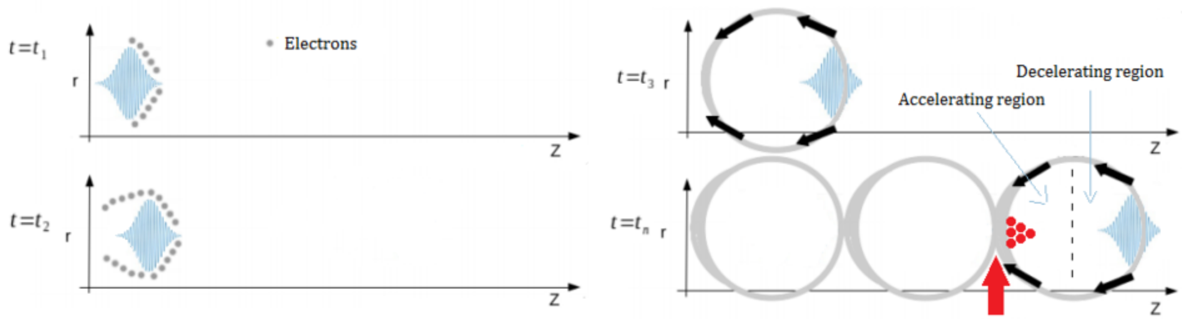

Figure 4: Time evolution of the wakefield in bubble regime in the plasma created by an intense laser pulse, moving in the z-direction with polarization plane in the r-direction, and the subsequent formation of a bundle of bubbles. At $t = t_1$, the electrons are expelled by the driver pulse while ions (entire white background) created a local positive region. At $t = t_2$, the electrons are attracted by the local positive region while the pulse is travelling. At $t = t_3$, the electron density form a bubble dragged by the pulse. At $t = t_n$, multiple bubbles are formed as a bubble train with a single driver pulse. The red arrow indicates the electron injection site for the most efficient acceleration. After these electrons pass beyond the dashed line, their phase no longer corresponds with the phase of the plasma wave and these electrons cannot be further accelerated.

pulse group velocity, which depends on the local plasma density, this does not provide rapid and accurate feedback for optimizing experimental parameters [4]. Apart from these markedly limiting factors, the FDI method provides a relatively high sensitivity even for small plasma density perturbations. Other diagnostic methods, their properties and advantages, are discussed in more detail in upcoming thesis.

References

[1] Tajima, T. and Dawson, J. M. Laser Electron Accelerator. In *Phys. Rev. Lett., (43)4*, pages 267–270. American Physical Society, *doi:10.1103/PhysRevLett.43.267*, 1979.

[2] Esarey, E. and Schroeder, C. B. and Leemans, W. P. Physics of laser-driven plasma-based electron accelerators. In *Rev. Mod. Phys., (81)3*, pages 1229–1285. American Physical Society, *doi:10.1103/RevModPhys.81.1229*, 2009.

[3] Lee, V. and Oganyan, B. A Brief Introduction to Plasma Accelerators. In *Journal of Undergraduate Reports in Physics, (28)1*, pages 1–4. 2009. *doi:10.1063/1.5109558*, 2018.

[4] Veisz, L. and Buck, A. and Nicolai, M. and Schmid, K. and Sears, Ch. M. S. and Sävert, A. and Mikhailova, J. M. and Kaluza, M. C. and Krausz, F. Diagnostics of electron beams and plasma wave in laser-plasma accelerators. In *AIP Conference Proceedings, (1507)1*, pages 111–119. *doi:10.1063/1.4773683*, 2012.

Study of equilibration of charm quarks in HYDJET++

Jaroslav Štorek

1 Introduction

In ultra-relativistic collisions of heavy nuclei, medium composed of deconfined quarks and gluons, quark-gluon plasma (QGP), can be created. Reproducing experimental results by the HYDJET++ Monte Carlo event generator can help scientific community to better understand properties of QGP and nature of the underlying processes. In this proceedings, simulation results of charged and charm particles with HYDJET++ model version 2.4 in Pb+Pb collisions at $\sqrt{s_{\rm NN}} = 2.76$ and 5.02 TeV and in Au+Au collisions at $\sqrt{s_{\rm NN}} = 200$ GeV energies are summarized. Transverse momentum spectra and flow harmonics have been studied for charged hadrons and D and J/ψ mesons.

2 HYDJET++

HYDJET++ is a Monte Carlo (MC) generator for simulation of symmetric relativistic heavy ion collisions. It includes a detailed treatment of soft hadron production and hard multi-parton production [1]. Hard production in a single nucleon-nucleon collision is obtained as modified jet event from the Fortran-based PYTHIA 6.4 generator [2]. The soft hadronic states of the HYDJET++ model are generated on the chemical and thermal freeze-out hypersurfaces obtained from hydro-inspired blast-wave parameterization with given freeze-out conditions as the boundary conditions.

2.1 Simulation Parameters

The HYDJET++ simulator is controlled by the input parameters. Every version of the HYDJET++ comes with already tuned or suggested sets of parameters for charged hadrons at specific collision energies. In the case of 2.4 version it is Au+Au collisions at $\sqrt{s_{\rm NN}} = 200$ GeV, Pb+Pb collisions at $\sqrt{s_{\rm NN}} = 2.76$ and Pb+Pb collisions at $\sqrt{s_{\rm NN}} = 5.02$ TeV. It has been found that the most influential parameters for the production of different species of the particles are:

- temperature at chemical freeze-out T_{ch},
- temperature at thermal freeze-out T_{th},
- minimal p_T of parton-parton scattering in PYTHIA event $p_{T,min}$,
- initial QGP temperature for central Pb+Pb collisions in midrapidity T_0.
- maximal longitudinal fluid flow rapidity at thermal freeze-out η_{max},
- maximal transverse fluid flow rapidity at thermal freeze-out for central collisions ρ_{max} and
- charmness enhancement factor γ_c

and their summary can be seen in Tab. 1. Overview of all the parameters can be found in the HYDJET++ documentation [1].

3 Results

Charged hadron and charm meson particle spectra in three collision and energy setups have been studied in this project: Au+Au collisions at $\sqrt{s_{\rm NN}} = 200$ GeV and Pb+Pb collisions at $\sqrt{s_{\rm NN}} = 2.76$ and 5.02 TeV.

system	Au+Au		Pb+Pb			
$\sqrt{s_{\rm NN}}$ [TeV]	0.2		2.76		5.02	
particle set	$h^{\pm}$	$D, J/\psi$	$h^{\pm}, D$	J/ψ	$h^{\pm}, D$	J/ψ
T_{ch} [GeV]	0.165	0.165	0.165	0.165	0.165	0.165
T_{th} [GeV]	0.1	0.165	0.105	0.165	0.105	0.165
$p_{T,min}$ [GeV/c]	3.55	3.55	8.2	3	10	5
T_0 [GeV]	0.3	0.3	1	1	1.1	1.1
η_{max}	3	1.1	4.5	2.3	4.5	2.3
ρ_{max}	1.1	0.5	1.265	0.6	1.35	0.6
γ_c	-1	7	11.5	11.5	15	15

Table 1: List of the HYDJET++ parameters used in Au+Au collisions at $\sqrt{s_{\rm NN}} = 200$ GeV and in Pb+Pb collisions at $\sqrt{s_{\rm NN}} = 2.76$ and 5.02 TeV for charged hadrons $h^{\pm}$ and charm hadrons J/ψ and D.

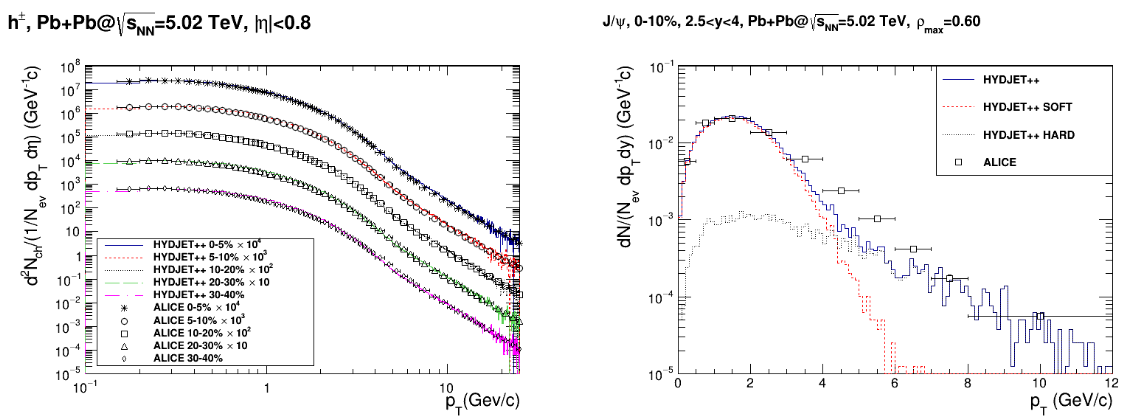

Figure 5: *Left:* The HYDJET++ simulated charged hadron $h^{\pm}$ yield p_T distributions in five centrality bins compared to the ALICE experimental data [3]. *Right:* Comparison of the HYDJET++ simulated p_T distribution histograms of the J/ψ meson yield to the ALICE experimental data [4] in 0-10% centrality region. The soft and hard HYDJET++ component have been extracted. Both graphs show Pb+Pb collisions at $\sqrt{s_{\rm NN}} = 5.02$ TeV.

In simulations of Au+Au collisions at $\sqrt{s_{\rm NN}} = 200$ GeV, simulation parameters tuned for HYDJET++ 2.1 version have been used. The HYDJET++ 2.1 version lacks calculation of intrinsic triangular flow reaction plane and further special v_2 and v_3 options. It has been found that the HYDJET++ 2.4 version is unable to correctly describe v_2 of charged hadrons and new tuning of the parameters is needed. In case of D mesons and J/ψ mesons, tuning of γ_c parameter, which scales the charm meson production, was needed to match the p_T distributions.

In simulations of Pb+Pb collisions at $\sqrt{s_{\rm NN}} = 2.76$ TeV, finely tuned parameters have been used as an input and correct description of all the distributions has been observed. Unlike Au+Au collisions at $\sqrt{s_{\rm NN}} = 200$ GeV, D mesons thermalize at the same temperature as the charged hadrons.

The highest energy $\sqrt{s_{\rm NN}} = 5.02$ TeV Pb+Pb collisions have been studied for the first time. It has been observed that suggested tuned parameters can describe well the observed spectra of charged hadrons $h^{\pm}$. Transverse momentum p_T spectra of charged hadrons $h^{\pm}$ for five centrality bins up to 40% centrality can bee seen in left Fig. 19. For correct description of charm mesons, tuning of γ_c parameter was needed. The tuning has been performed on J/ψ yield in 0-10% centrality bin and the result with $\gamma_c = 15$ can be seen in right Fig. 19. Dependence of the J/ψ transverse momentum p_T, elliptic flow v_2 and triangular flow v_3 on the fluid flow transverse rapidity parameter ρ_{max} has been also studied and no significant improvement of the spectra with respect to the default value $\rho_{max} = 0.6$ has been observed.

4 Conclusion

Transverse momentum spectra and flow coefficients of charged particles and charm mesons has been simulated with HYDJET++ event generator in three collisions setups and compared to experimental data. It has been found that new tuning of the simulation parameters is needed for Au+Au collisions at $\sqrt{s_{\mathrm{NN}}} = 200$ GeV and that Pb+Pb collisions can be described well by the suggested parameters at $\sqrt{s_{\mathrm{NN}}} = 2.76$ TeV. Tuning of the parameters for charm mesons in Pb+Pb collisions at $\sqrt{s_{\mathrm{NN}}} = 5.02$ TeV has been performed and correct description of the experimental data has been achieved in the most central collisions.

References

[1] I. P. Lokhtin et al. Heavy ion event generator HYDJET++ (HYDrodynamics plus JETs). Comput. Phys. Commun., 180(5):779, May 2009. doi:10.1016/j.cpc.2008.11.015.

[2] T. Sjöstrand et al. Pythia 6.4 physics and manual. J. High Energy Phys., 2006(05):26, May 2006. doi:10.1088/1126-6708/2006/05/026.

[3] S. Acharya et al. Transverse momentum spectra and nuclear modification factors of charged particles in pp, p-Pb and Pb-Pb collisions at the LHC. J. High Energy Phys., 11:013, 2018. doi:10.1007/J.HighEnergyPhys.11(2018)013.

[4] S. Acharya et al. Studies of J/ψ production at forward rapidity in Pb–Pb collisions at $\sqrt{s_{\mathrm{NN}}}$ = 5.02 TeV J. High Energy Phys., 2020(2):41, Feb 2020. doi:10.1007/J.HighEnergyPhys.02(2020)041.

INCOHERENT PHOTOPRODUCTION OF J/ψ IN ULTRA-PERIPHERAL PB-PB COLLISIONS WITH ALICE

David Grund

1 Introduction

The analysis of diffractive photoproduction of vector mesons in ultra-peripheral collisions (UPCs) [1] of heavy ions at the LHC offers an efficient way to probe the structure of nuclei at low Bjorken-x. It enables one to examine the effects of high-energy QCD phenomena such as nuclear shadowing or gluon saturation, which are nowadays actively researched. In particular, with the incoherent photoproduction, one can study event-by-event fluctuations of the transverse structure of nucleons.

2 Analysis of Run 2 data

In this talk, the analysis of the incoherent photoproduction of J/ψ mesons in Pb–Pb collisions at the centre-of-mass energy of $\sqrt{s_{\mathrm{NN}}} = 5.02$ TeV with ALICE was presented. The J/ψ mesons were reconstructed from the decays into muon pairs at midrapidity, $|y| < 0.8$, using the information from the main tracking central-barrel ALICE detectors, the ITS and the TPC. The events were triggered by the central UPC trigger, which was based on the input data from the TOF, V0 and AD detectors.

The raw yield of J/ψ candidates in the incoherent-enriched sample ($p_{\mathrm{T}} > 0.2$ GeV/c) was extracted from the fit of the invariant mass distribution of muon pairs, see Fig. 6. The yield was found to be about seven times higher than in the previous ALICE measurement of the midrapidity incoherent J/ψ photoproduction at $\sqrt{s_{\mathrm{NN}}} = 2.76$ TeV [2]. The feed-down contamination of the incoherent-enriched sample was calculated using the MC data samples generated in STARlight [3] and the contamination from coherent events was determined by means of the fit of the transverse momentum distribution of measured events in the range $p_{\mathrm{T}} < 2$ GeV/c, see Fig. 7.

3 Conclusion

The first estimate of the incoherent photoproduction cross section per unit rapidity was determined as (0.69 ± 0.03) (stat.) mb. Owing to the increase in the raw yield of J/ψ candidates, the relative statistical uncertainty was substantially reduced with respect to the previous ALICE measurement. This enables one to perform more detailed studies devoted to the sources of various systematic errors, which were left for future work.

References

[1] J.G. Contreras, J. D. Tapia Takaki: Ultra-peripheral heavy-ion collisions at the LHC. International Journal of Modern Physics A 30(8), 1542012 (2015).

[2] E. Abbas et al.: Charmonium and e^+e^- pair photoproduction at mid-rapidity in ultraperipheral Pb–Pb collisions at $\sqrt{s_{\mathrm{NN}}} = 2.76$ TeV. Eur. Phys. J. C 73.11, p. 2617 (2013).

[3] S. R. Klein, J. Nystrand, J. Seger, Y. Gorbunov, and J. Butterworth: STARlight: A Monte Carlo simulation program for ultra-peripheral collisions of relativistic ions. Comput. Phys. Commun. 212, 258–268 (2017).

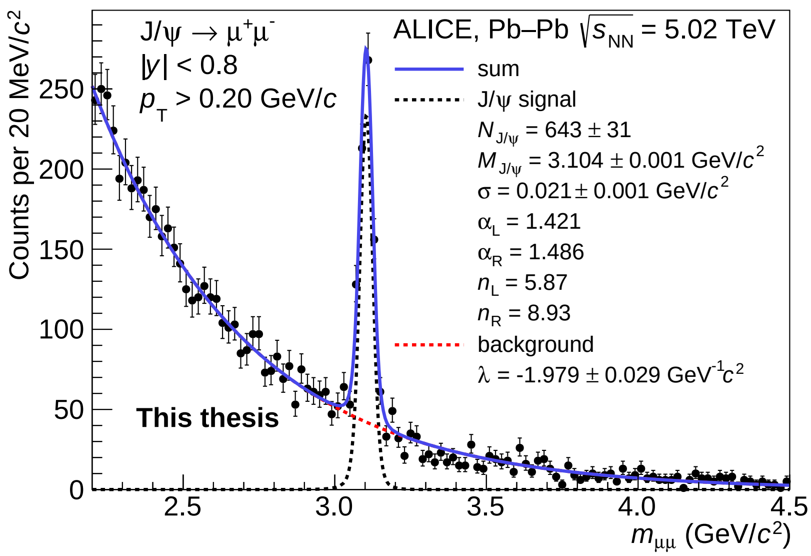

Figure 6: Fit of the invariant mass distribution of dimuons from the incoherent-enriched sample.

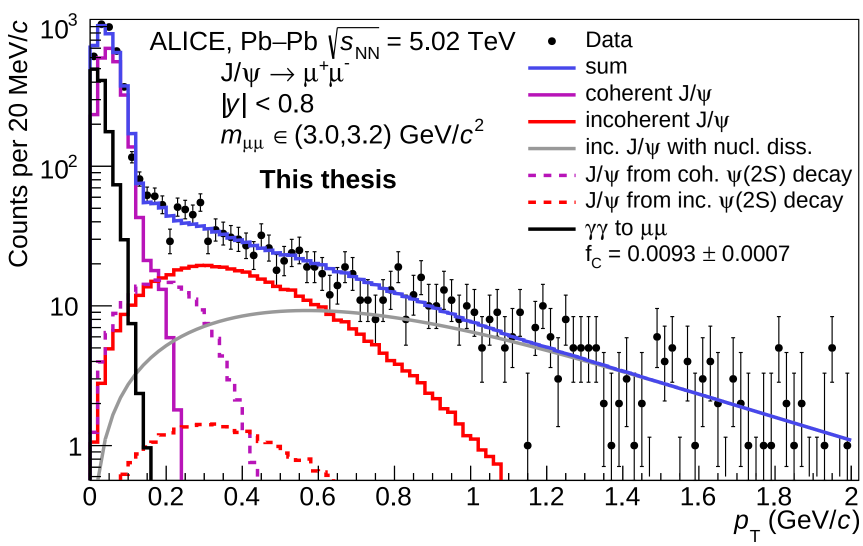

Figure 7: Fit of the transverse momentum distribution of measured events with $3.0 < m_{\mu\mu} < 3.2$ GeV/c^2 and $|y| < 0.8$.

Initial conditions for hydrodynamic simulations of collisions at RHIC-BES energies

Jakub Štěrba

1 Introduction

When two heavy ions collide, if sufficient energy density and temperature is reached, the quark-gluon plasma (QGP) is produced. This quark-gluon plasma then subsequently undergoes a collective expansion and eventually becomes so dilute it hadronizes. This collective expansion is called flow.

2 Collective flow

Flow is an observable which gives us information about the equation of state and the transport properties of the quark-gluon plasma. The clearest experimental signature of collective flow is the azimuthal anizotropy in particle production. The initial asymmetry in the geometry of the system, which can be caused by e.g. non-central collisions, cause so-called anisotropic flow. One of the components of the anisotropic flow is elliptic flow.

After the collision, the QGP is produced in so-called almond shape. But during the evolution the spatial anisotropy vanishes, whille the anisotropy in momentum space changes to the opposite direction. This momentum anisotropy is dependent on the equation of state of the medium and this dependence is reflected in the elliptic flow.

3 The used codes

3.1 Glissando

Glissando is a Monte Carlo Glauber simulation of the initial stages of the heavy-ion collisions. Basically it generates the two dimensional energy density profile of the fireball. Here, fireball is meant as distribution of all spatial destributions of the transverse enregy (all sources). The output from Glissando is static and it can be used for the studies of the shape of the medium, e.g. hydrodynamic studies.

3.2 vHLLE

vHLLE is the 3+1 dimensional relativistic hydrodynamic code. It transforms the matter from the initial state into fluid, which is evolved by solving relativistic viscous hydrodynamic equations until the freeze-out. The main advantage of this code is that the common assumption of boost-invariant longitudinal expansion and zero net baryon density in the entire system are relaxed. This relaxation is good for simulation of the collisions at RHIC-BES energies.

4 The task

For the task hybrid vHLLE package is used, which aside from vHLLE cantains also hadronSampler code, which basically forms an re-scatters hadrons after the end of the hydrodynamic evolution. As initial conditions, Glissando is used.

The setup described above is was used to simulate RHIC BES collisions, but resulting elliptic flow did not match the values of elliptic flow presented by the STAR Collaboration [1], for $|p_T| > 1$ GeV.

As a first try to add the elliptic flow, initial transverse velocity was added to each cell of hydrodynamic grid. The velocity is given by

$$v(r,\phi) = \zeta\left(\frac{r}{r_{max}}\right)^2 (1 + 2a\cos 2\phi) + v_{rand}; \qquad |v(r,\phi)| < 1, \tag{2}$$

r is the radial coordinate in the transverse plane, ϕ is the azimuthal angle and v_{rand} stands for random component given by normal distribution with parameters σ, μ. r_{max} is set to 3.5 fm, since it is a typical size of the fireball after the hydrodynamic evolution. The condition for the velocity to be smaller than 1 is kept. ζ and a are parameters of the model which are needed to be estimated.

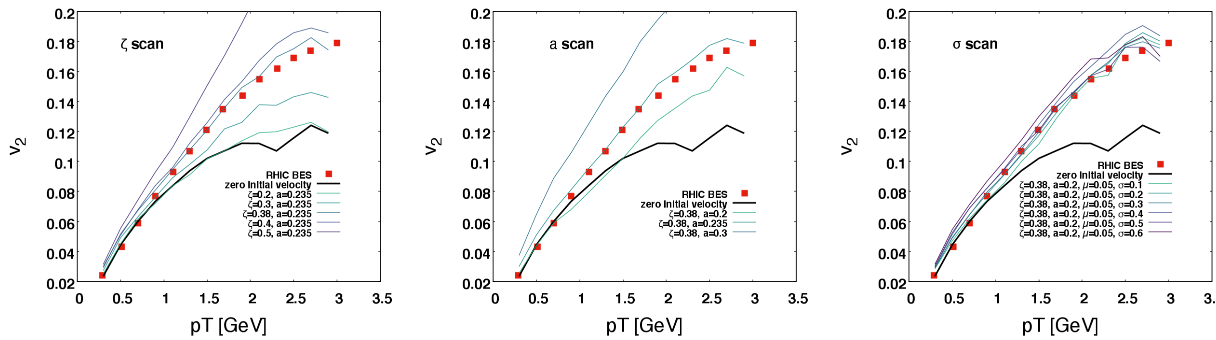

Figure 8: Sample figure caption.

In the Fig. 1 can be seen the results at the centrality $20-30\%$ and $\sqrt{s_{NN}} = 27$ GeV. The plots show scans for individual parameters ζ, a and σ. The black solid line represents the elliptic flow from the simulation with no initial velocity added and the red points represent data from RHIC BES [1].

It can be seen (left plot) that increasing the ζ leads to the increase of the magnitude of the elliptic flow v_2 as well. Similar behaviour has the increasing of the a parameter (middle plot). On the other hand, change of the σ parameter has no dramatic effect (right plot). For all σ scan was μ set to 0.05 in order to have rather possitive addition.

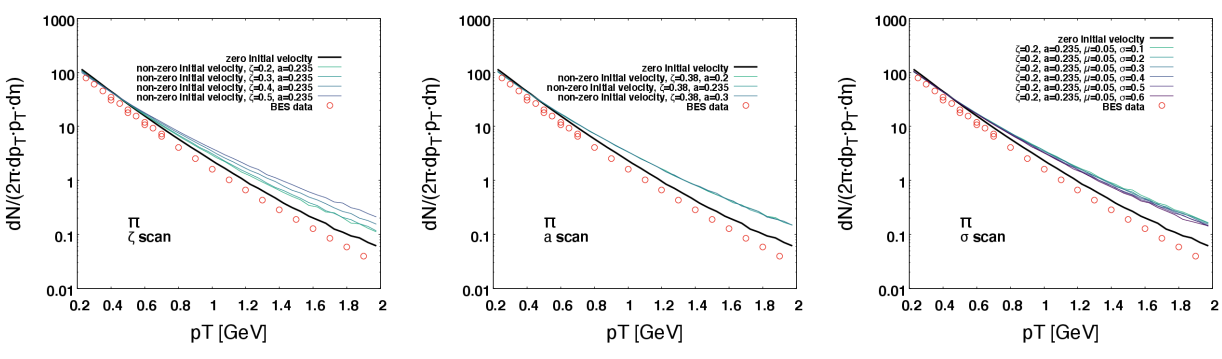

Figure 9: Sample figure caption.

For the same values of parameters from Fig. 1, there were p_T spectra plotted (Fig. 2).

Here, in fact, can be seen nice behaviour when changing the parameters. Increasing ζ flattens the spectrum while changing a has no effect on the spectrum. This behaviour is good because ζ parameter can be set accordingly to the spectrum and a can be set to reproduce the elliptic flow. The σ has no big effect on the spectrum, just a small increase of tho slope, since the collectivity is probably violated if σ is increased.

However, the p_T spectrum which matches the spectrum from RHIC BES [2] the best is the spectrum with no initial velocity added. In fact, adding the initial velocity spoils the spectrum. That is why some further steps are needed, such as starting the hydrodynamic evolution later or decreasing the energy density at which the hydrodynamics stops.

References

[1] L. Adamczyk *et al.*, *Inclusive charged hadron elliptic flow in Au + Au collisions at* $\sqrt{s_{NN}}$ *= 7.7 - 39 GeV*, Phys. Rev. C **86** (2012), 054908 doi:10.1103/PhysRevC.86.054908 [arXiv:1206.5528 [nucl-ex]].

[2] L. Adamczyk *et al.*, *Bulk Properties of the Medium Produced in Relativistic Heavy-Ion Collisions from the Beam Energy Scan Program*, Phys. Rev. C **96** (2017) no.4, 044904 doi:10.1103/PhysRevC.96.044904 [arXiv:1701.07065 [nucl-ex]].

[3] R. Snellings, *Elliptic Flow: A Brief Review*, New J. Phys. **13** (2011), 055008 doi:10.1088/1367-2630/13/5/055008 [arXiv:1102.3010 [nucl-ex]].

[4] W. Broniowski, M. Rybczynski and P. Bozek, *GLISSANDO: Glauber initial-state simulation and more..*, Comput. Phys. Commun. **180** (2009), 69-83 doi:10.1016/j.cpc.2008.07.016 [arXiv:0710.5731 [nucl-th]].

[5] I. Karpenko, P. Huovinen and M. Bleicher, *A 3+1 dimensional viscous hydrodynamic code for relativistic heavy ion collisions*, Comput. Phys. Commun. **185** (2014), 3016-3027 doi:10.1016/j.cpc.2014.07.010 [arXiv:1312.4160 [nucl-th]].

Systematic uncertainty of mass composition of cosmic rays interpreted from measurements of depth of shower maximum using different Monte Carlo generators

Karolína Syrokvaš

1 Systematic uncertainty of mass composition

The mass composition of cosmic rays plays a crucial role in the knowledge of the origin of high-energy cosmic rays. [1] Mass spectrum of energies up to 10^{14} eV can be measured directly, whereas for higher energies, one observes extensive air showers (EAS), where the mass of the primary particle can only be obtained from comparisons of experimental observables with air shower simulations. These, however, are subject to uncertainties of hadronic interactions at the highest energies, especially for energies higher than those attainable at particle accelerators. This means that for energies above 10^{20} eV, accelerator data need to be extrapolated. The model uncertainties are the dominant source of systematic uncertainties of the mass composition at the highest energies.

By producing simulations of 5000 showers for different primaries (protons, helium, oxygen and iron nuclei) and fitting the distributions of shower maximum X_{max} at the Pierre Auger Observatory (PAO) using the generated distribution for each primary, one can estimate the fractions of fitted primaries. Simulations were run on the computer farm Goliáš of the Institute of Physics of the Czech Academy of Sciences. The simulation programme is CORSIKA compiled with hadronic interaction models Sibyll 2.3c, EPOS LHC and GSJET-II 04. The energy range for the simulations is $10^{18.5}$ – 10^{19} eV, and four different atmosphere models are also used in these simulations, along with already existing CONEX simulations in the Goliáš computer farm, where nitrogen primary is used instead of oxygen.

2 Models of hadronic interactions

The selection of a model of hadronic interactions affects resulting observables of the shower, changing the number of muons produced or the depth of the shower maximum. When drawing conclusions of the mass composition, it is important to know which models describe experimental data with best accuracy. Usually more than just one hadronic interactions model is used when identifying the composition of experimental data.

Sibyll 2.3c Sibyll is one of the first hadronic interactions models created specifically for the interpretation of the cosmic ray data. [2] The development of this event generator started already in the late 1980. A large quantity of shower simulations were done with Sibyll, most importantly all simulations used for designing PAO. From the history of air shower simulations, this model uses simplifications affecting the results in a way that makes it inferior to other, more advanced models. On the other hand, these simplifications shorten the time needed to compute the shower.

QGSJET-II 04 The QGSJET model uses Quark-Gluon String model and enhanced Pomeron diagrams. [4] . The greatest disadvantage of this model is its complexity, making it susceptible to development of mistakes. This model is also, from the three models mentioned, the one predicting the shower depth maxima measured at PAO the worst.

EPOS LHC EPOS is currently one of the most advanced hadronicic models to date. [3] The Hadronic interactions model EPOS LHC takes into account nuclear interactions during the collisions, fits well data from RHIC and LHC. This model produces more muons on ground than the previously mentioned QGSJET-II 04 or Sibyll 2.1, but still less than Sibyll 2.3c. The cost of such sofisticated model has, however, somewhat longer simulation time, rendering this model not very practical for quick computations.

3 Simulation programs

CONEX CONEX is one-dimensional hybrid air shower simulation program. [5] This means that the shower is described using cascade equations, using Monte Carlo only at the most energetic part of the shower. This strategy reduces the computation demands. While this hybrid approach is the main idea of CONEX, it can run in full Monte Carlo mode.

CORSIKA CORSIKA, short for COsmic Ray SImulations for KAscade, is a Monte Carlo program for high energies [6]. It creates three-dimesional simulations that have higher demands on computation time with higher energies of the primary particle than in the case of CONEX. To reduce these demands, CORSIKA has so-called thinning energy E_{thin}, from which it does thin sampling. Thinning means that CORSIKA explicitly simulates only a small fraction of all particles and assigns them a weight factor. When the shower reaches the phase where a great number of particles is produced, one of the secondary particles is randomly selected as a representative of the rest, which is discarded. This approach reduces computing time but raises uncertanities of observables, meaning that the optimal E_{thin} needs to be selected for the individual purposes of a simulation.

4 Figures

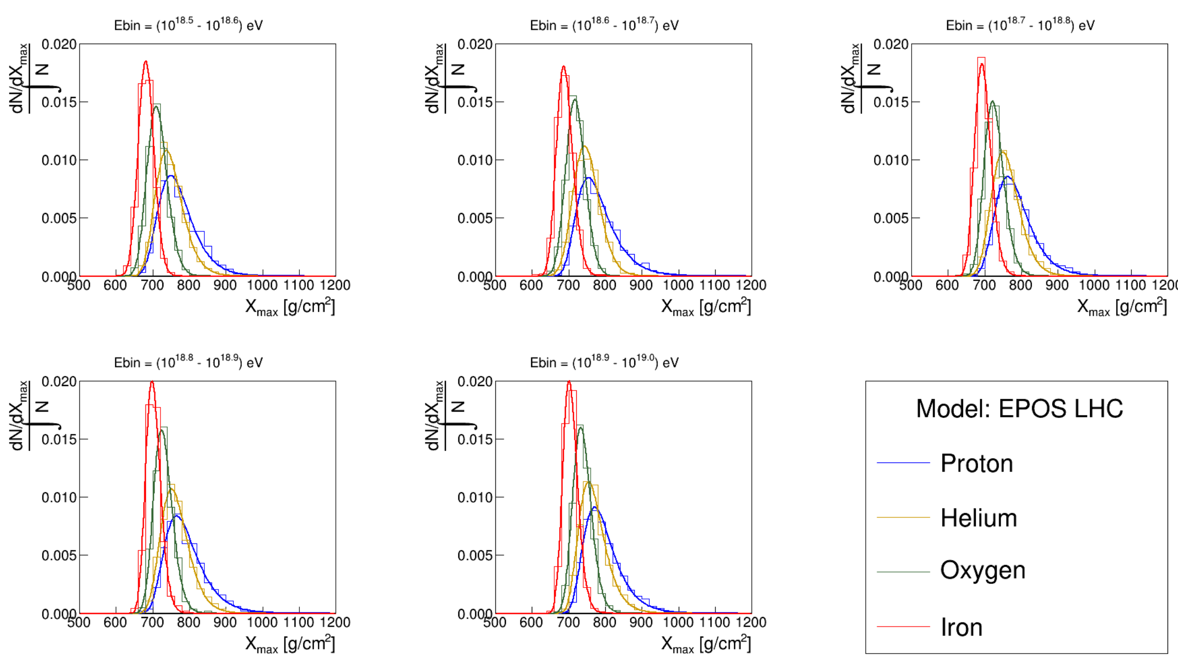

Figure 10: Simulated spectra of proton, helium, oxygen and iron primaries using model EPOS LHC in CORSIKA. Histograms are normalized and fitted using Generalized Gumbel distribution: $\frac{1}{\sigma} \cdot \frac{\lambda^\lambda}{\Gamma(\lambda)} \cdot e^{-\lambda \cdot \frac{x-\mu}{\sigma} - \lambda \cdot e^{-\frac{x-\mu}{\sigma}}}$.

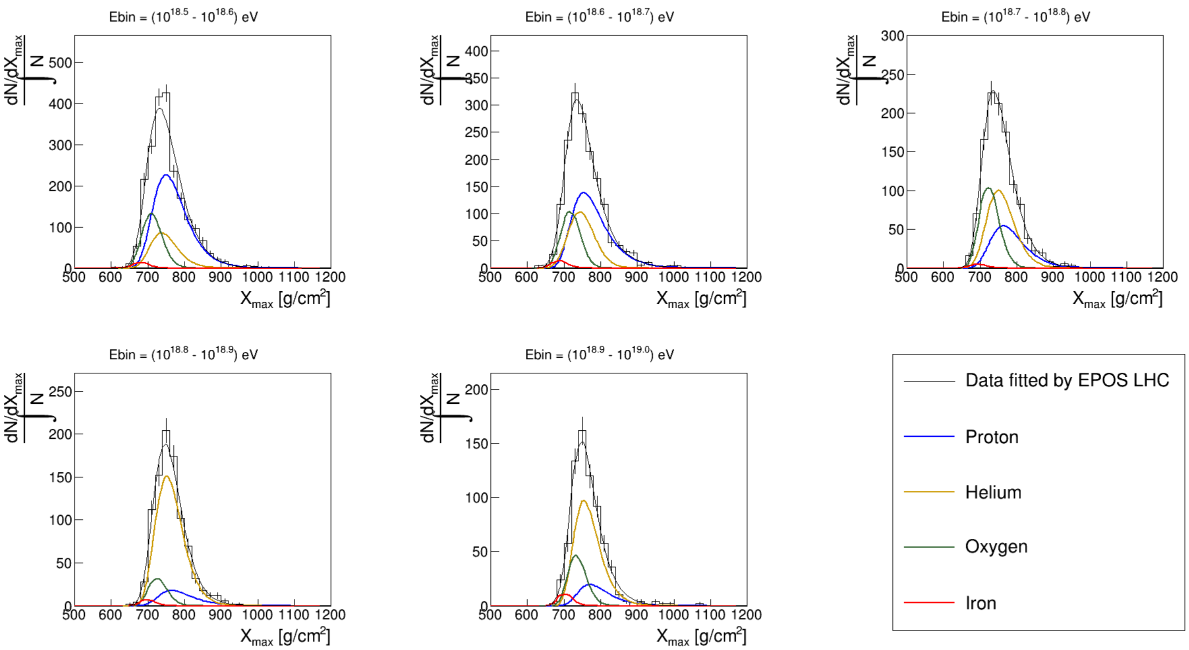

Figure 11: Real data detected by PAO, fitted using the distributions fitted by simulations.

References

[1] K.-H. Kampert, M. Unger: *Measurements of the Cosmic Ray Composition with Air Shower Experiments* [Online]. [cit. 11. 1. 2020]. `https://arxiv.org/pdf/1201.0018.pdf`.

[2] Engel, Ralph & Riehn, Felix & Fedynitch, Anatoli & Gaisser, Thomas & Stanev, Todor: *The hadronic interaction model Sibyll – past, present and future* [Online]. [cit. 11. 1. 2020]. `https://www.researchgate.net/publication/317901448_The_hadronic_interaction_model_Sibyll_-_past_present_and_future`.

[3] T. Pierog, K. Werner: *EPOS Model and Ultra High Energy Cosmic Rays* [Online]. [cit. 11. 1. 2020]. `https://arxiv.org/pdf/0905.1198.pdf`.

[4] S. Ostapchenko, D. Heck: *Hadronic Interactions in QGSJET-II: Physics and Results* [Online]. [cit. 11. 1. 2020]. `https://cds.cern.ch/record/965306/files/17135-ger-ostapchenko-S-abs1-he14-oral.pdf`.

[5] T. Bergmann, R. Engel, D. Heck, N. N. Kalmykov, S. Ostapchenko, T. Pierog, T. Thouw, K. Werner: *One-dimensional Hybrid Approach to Extensive Air Shower Simulation* [Online]. [cit. 12. 1. 2020]. `https://arxiv.org/pdf/astro-ph/0606564.pdf`.

[6] D. Heck, J. Knapp: *Upgrade to the Monte Carlo Code CORSIKA to Simulate Extensive Air Showers with Energies* $> 10^{20}$ *eV* [Online]. [cit. 12. 1. 2020]. `http://inspirehep.net/record/475981/files/FZKA6097.pdf`.

Global polarization of lambda hyperons in heavy-ion collisions at STAR

Ondřej Lomický

1 Global Λ polarization

Lambdas or antilambdas which are produced in heavy-ion collisions can reveal some properties of quark-gluon plasma (QGP). The QGP can have a non-zero global angular momentum $\vec{J}$ which can be measured via the lambdas. Their spin prefers the direction of the angular momentum $\vec{J}$. However, these particles have zero electric charge and relatively short mean lifetime $\tau = (2.632 \pm 0.020) \cdot 10^{-10}$ s. Therefore their daughter particles protons and related pions are measured instead of the mother particles. The next important property of lambdas is that they are the so-called 'self-analysis', i.e. the daughter proton prefers the direction of the mother particle's spin. Hence, one can reconstruct the angular momentum of the QGP via the aforementioned protons. The first step is to measure the global lambda polarization. The polarization means an alignment of the spin with the direction of the angular momentum $\vec{J}$.

The three coupled results from the different analyses which were published in 2007, 2017 and 2018 can be seen in Fig. 12. The recent results for energy $\sqrt{s_{\rm NN}} = 200$ GeV reveal non-zero polarization.

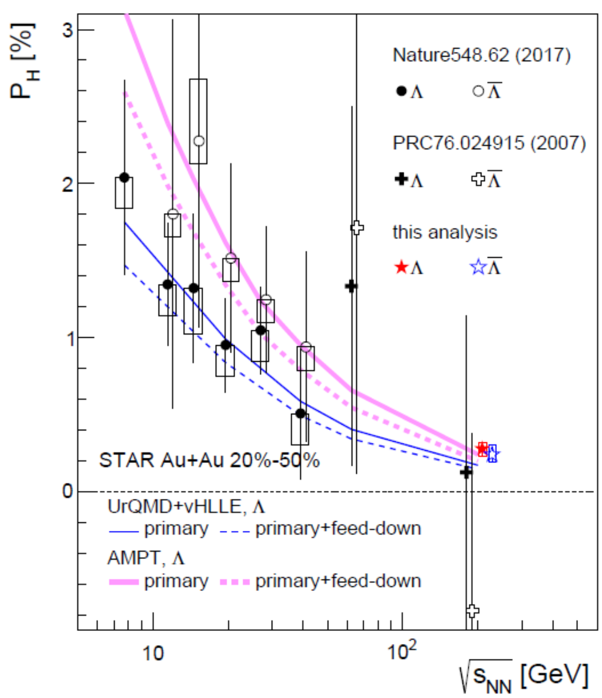

Figure 12: Global polarization of Λ and $\overline{\Lambda}$ as a function of the collision energy $\sqrt{S_{\rm NN}}$ for 20-50% centrality Au+Au collisions [1].

The global angular polarization P_H can be obtained by

$$P_H \equiv \frac{8}{\pi \alpha_H} \frac{\langle \sin(\Psi_1 - \phi_p^*) \rangle}{\mathrm{Res}(\Psi_1)}, \tag{3}$$

where α_H is a decay parameter ($\alpha_\Lambda = -\alpha_{\overline{\Lambda}} = 0.642 \pm 0.013$), Ψ_1 is an azimuthal angle of the angular momentum of the first-order event plane, ϕ_p^* is an azimuthal angle of the daughter proton in the rest frame of Λ and Res(Ψ_1) means resolution of the EP of the first order.

2 Event plane

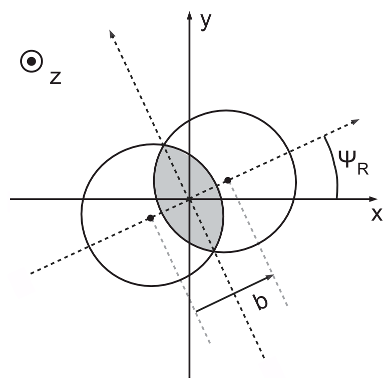

Figure 13: The angle of reaction plane Ψ_R with respect to x-axis where b is an impact parameter [2].

The reaction plane (RP) is defined by the impact parameter of two nuclei b and beam axis as is shown in Fig. 13. However, the impact parameter can not be measured directly thus the RP is also directly immeasurable. The event plane (EP) is an estimation of the RP of the first order and it can be computed as follows:

$$\Psi_1 = \arctan\left(\frac{Q_{(1,y)}}{Q_{(1,x)}}\right) = \arctan\left(\frac{\sum_i w_i \sin\phi_i}{\sum_i w_i \sin\phi_i}\right) \tag{4}$$

where $\vec{Q}_1$ is the so-called Q-vector of the first order, ϕ_i is an azimuthal angle of the i-th particle and w_i is the weight for related particle. In general, the weight is chosen to maximize the resolution of the EP.

If one considers a real detector then a couple of corrections have to be taken into account. For instance which is related to the fact that not all of the tiles of the detector have the same sensitivity and psi-shifting which is used to flatten the Ψ_1 distribution. The resolution of the EP is given by

$$\mathrm{Res}(\Psi_1) = \langle \cos(\Psi_1 - \Psi_R) \rangle \tag{5}$$

where the angle brackets denote the mean value for a large sample of events.

3 Reconstruction of Λ hyperons

The lambdas can be reconstructed via Kalman filter for particle finder which uses covariance matrix and state vectors of measured particles. Topological cuts (e.g. distance of closest approach (DCA) between tracks of daughter particles) are applied to maximize the probability that the reconstructed particles were real lambdas. The daughter protons can be boosted into the rest frame of the mother particle after the reconstruction. The angle of the boosted daughter baryons together with EP and its resolution (see Eq. (3)) can show the global polarization of lambdas. However, some particles are improperly reconstructed and these fake lambdas can influence the polarization. One can use invariant mass method or event plane method to clean the measured polarization. The final Λ polarization indicates vorticity of $\omega \approx (9 \pm 1) \times 10^{21}$ s^{-1} which is the highest value of vorticity which have been ever observed in the Universe [3].

References

[1] Anon, (2018). Researchgate. [online] Available at: https://www.researchgate.net/publication/325118641_Global_polarization_of_Lambda_hyperons_in_AuAu_collisions_at_sqrts_NN_200_GeV [Accessed 12 Jan. 2020].

[2] CHATRCHYAN, S., V. KHACHATRYAN, A. M. SIRUNYAN, et al. Physical Review C. 2013, 87(1). ISSN 0556-2813. Available at:https://journals.aps.org/prc/pdf/10.1103/PhysRevC.87.014902

[3] Global Λ hyperon polarization in nuclear collisions. Nature [online]. 2017, 548(7665), 62-65 [cit. 2021-5-2]. ISSN 0028-0836. Available at:: https://arxiv.org/pdf/1701.06657.pdf

Identifying Heavy-Flavor Jets Using Vectors of Locally Aggregated Descriptors

Georgij Ponimatkin

1 Introduction

Accurate identification of heavy-flavor jets is an important task that is crucial to many physical measurements, for example new physics searches via boosted object decays or studies of flavor dependence of parton energy loss in dense nuclear medium. To precisely study heavy-flavor jets one needs a vast amounts of data, due to their reduced cross-section with respect to the light-flavor jets. Another factor that leads to the scarcity of heavy-flavor jets is stemming from the complicated experimental reconstruction. Traditional methods deal with reconstruction based on vertex related statistical templates, which tend to have low performance.

2 JetVLAD tagger

With recent rise of modern machine learning techniques the question arises - to what extend can we improve the tagging performance by utilizing state-of-the-art machine learning techniques? To find this out, as part of my master thesis research I have developed a novel heavy-flavor jet tagging algorithm called JetVLAD [1], which is based on the NetVLAD layer [2]. The model was developed mainly for p+p collisions at $\sqrt{s} = 200$ GeV, but the approach should be applicable to different energies as well. The efficiency vs. purity graph that shows performance of our model at various jet p_T is shown in Fig. 14.

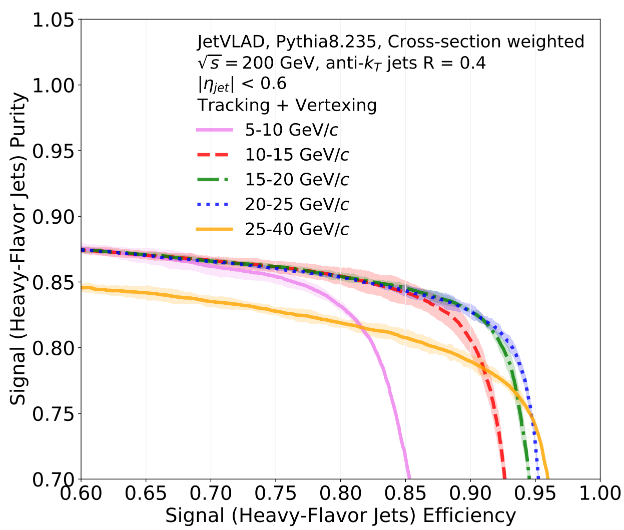

Figure 14: Efficiency vs. purity graph for heavy-flavor jet identification. Different colours represent different jet p_T. Taken from [1].

3 Conclusions

The applications of machine learning towards heavy-flavor jet identification is an active area of research that promises better utilization of the available data and hence more precise measurements. The recently introduced JetVLAD model is one such model, which achieves a great performance in heavy-flavor jet identification down to the low p_T. Such performance opens up a possibility to search for heavy-flavor jet radition patterns at lowest p_T, which might unveil a lot of information about internal structure of Quantum Chromodynamics.

References

[1] J. Bielcikova, R. Kunnawalkam Elayavalli, G. Ponimatkin, J. H. Putschke, and J. Sivic, Identifying Heavy-Flavor Jets Using Vectors of Locally Aggregated Descriptors, JINST, vol. 16, no. 03, P03017, 2021. arXiv: 2005.01842 [hep-ph].

[2] R. Arandjelovic, P. Gronat, A. Torii, T. Pajdla, and J. Sivic, Netvlad: CNN architecture for weakly supervised place recognition, CoRR, vol. abs/1511.07247, 2015. arXiv: 1511.07247.

AZIMUTHAL ASYMMETRIES IN COHERENT PHOTOPRODUCTION OF J/ψ WITH ALICE

Sára Haidlová
Faculty of Nuclear Sciences and Physical Engineering, Czech Technical University in Prague, Czech Republic

1 Introduction

One of the most studied problems in quantum chromodynamics is the gluon structure of hadrons and its behaviour. The nature of this problem is studied via deep-inleastic scattering, which provides a good instrument to probe the hadron structure. Processes frequently used for hadron photoproduction and studying the hadron structure are ultra-peripheral collisions (UPCs), specially high energy UPCs.

2 Ultra-peripheral collisions

Ultra-peripheral collisions occur for impact parameters larger than the sum of radii of nuclei. Given the large impact parameter of the interaction no hadronic interactions occur and particles interact solely through their electromagnetic fields. As particles get accelerated, their electromagnetic fields get Lorentz contracted. These fields can be considered to be a source of quasi-real photons, that are linearly polarized. The occurring processes can be classified into two groups, photon-photon interactions that are interactions between photons from the field of each nuclei. The second occurs when a photon from the electromagnetic field fluctuates into a quark-antiquark pair that subsequently scatters of a nucleus and emerges most likely as vector meson. The process of vector-meson photoproduction is sensitive to the gluon content of the hadron. The measurements are conducted at high energy,thus the distributions are studied at low Bjorken-x, for which the number of partons rises and the partons are virtual quark-antiquark pairs and gluons, hence the depence on the gluon content. Measurements of the scattering angle of the J/ψ allow for further studies of the evolution in Bjorken-x of the structure of hadrons.

3 Previous measurements

The coherent photoproduction of J/ψ is of particular interest. This is a process where the photon interacts with the whole nucleus, not with its individual parts. Previous measurements have been conducted at the LHC not only of coherent J/ψ photoproduction, but also incoherent and electron-positron pair production using data from 2011 on ultra-peripheral Pb-Pb collisions at $\sqrt{s_{NN}}$ = 2.76 TeV were analysed. The analysis provides information about the sensitivity of J/psi photoproduction to nuclear shadowing effects. Measured results are shown in Fig.19.

Other important phenomena that was previously studied is the azimuthal asymmetry that was studied in measurements of exclusive electron-positron pairs created by the Breit-wheeler process. The measurement was conducted by the STAR Collaboration at the Relativistic Heavy Ion Collider using Au-Au collisions at $\sqrt{s_{NN}}$ = 200 GeV with data from 2010. The results provide proof of the existence of an azimuthal asymmetry between the leptons from $\gamma\gamma$ interaction. The measurement was carried out in UPCs and central collisions, where $\cos 4\Delta\phi$ shows a 6.7σ significance. Measured results are shown in Fig.16.

4 ALICE

Related measurements can be carried out with ALICE (A Large Ion Collider Experiment). The necessary detectors can be divided into two groups , detectors in the central barrel, concretely Inner Tracking System, Time-Projection Chamber and Time-of-Flight detector. The Inner Tracking system surrounds the beam pipe and consists of 6 layers of silicon detectors with high precision. The ITS is used for primary and secondary vertex reconstruction and particle identification and tracking. The TPC is used for measurements of track momenta and particle identification and vertex determination. It is composed of a cylindrical field cage filled with a gas mixture. The TOF in combination with TPC and ITS also serves for particle identification by measuring the time of flight of a particle over a given distance. The second group are detectors is located in the forward region, concretely the V0 detector, Zero Degree caloremeter and ALICE diffractive detector. The V0 detector consists of V0A and V0C scintillator counters and can be used as a minimum-bias trigger for central barrel detector. Furthermore it serves as a centrality indicator and is used for luminosity measurements. ALICE further uses two sets of ZDCs for measurements of the energy of non-interacting nucleons. The ALICE diffractive detector is a scintillating detector and is placed in the very forward region. The AD detector can be used as a veto trigger for ultra-peripheral events to suppress background.

5 Figures

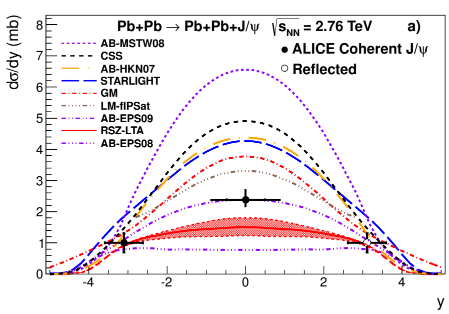

Figure 15: Measured differential cross section of J/ψ photoproduction in ultra-peripheral collisions for coherent events.[1]

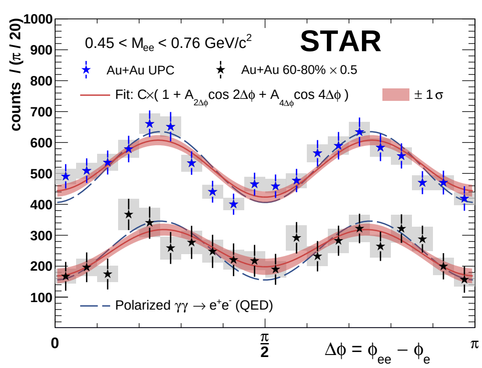

(1).pdf

Figure 16: Comparison of the $\Delta\phi = \phi_{ee} - \phi_e$ distribution from $60-80\%$ central Au+Au collisions with that in UPCs. The $\cos 4\Delta\phi$ modulation extracted from a fit to the $\Delta\phi$ distribution is shown along with the $\pm 1\sigma$ uncertainty band. [2]

References

[1] E. Abbas *et al.* [ALICE], Eur. Phys. J. C **73** (2013) no.11, 2617 doi:10.1140/epjc/s10052-013-2617-1 [arXiv:1305.1467 [nucl-ex]].

[2] J. Adam *et al.* [STAR], [arXiv:1910.12400 [nucl-ex]].

FEATURES OF UHECR SOURCES FOR HEAVY ENERGY TAIL

Bsc. Robert Hruby

1 Abstract

This research project is dedicated to the simulation propagation of extra-galactic UHECR in the universe using a simulation framework program called CRPropa 3 [**?**]. In high energy astronomy, the abbreviation UHECR stands for Ultra High Energy Cosmic rays, which could be any propagating particle with its energy exceeding the value of 1 EeV ($5\mathrm{x}10^{19}$ eV), "also the so-called Greisen-Zatsepin-Kuzmin limit" [**?**].

The first part of the research task, which will eventually prolong itself into a master thesis, is to look at the very end of the cosmic ray energy spectrum, also called the heavy energy tail. Here an interesting phenomenon can be found. It was initially observed and measured by Pierre Auger Observatory and what this project will try to do is to recreate the phenomenon that was observed in Xmax. [**?**]

Slant depth, which refers to the amount of material penetrated by the shower at a given point in its development, is also denoted as X, then the specific depth where is the highest number of particles is denoted as Xmax. In addition the place where the phenomenon was observed is the anisotrophy in these Xmax data. It is observed that those Xmax values are pointing at different values of anisotrophy for particles that are coming from different sources. In this case, particles that are from elsewhere beside the galactic disk. These particles appear heavier, causing them to be trapped for a longer period of time in the magnetic field of our galactic disk.

This project is then focused more on the simulation part where is trying to work with the initial conditions outside the galactic disk, which is then resulting in some final properties of the shower. This is then eventually a variable that will be changed many times up till the point it will come close to the data that were observed by Pierre Auger Observatory as a final product of the shower. This allows to trace back and find the initial properties of those showers, such as its mass composition, smearing of the arrival direction, its mixing, and so on.

As already mentioned the simulation framework program that is used in called CRPropa 3, it is a publicly available simulation framework, it is mainly used for the study of the propagation of ultra high energy nuclei on their voyage through (extra)galactic environment, where is considering most of the effects that are bound to come to its path. "Such as pion production, photodisintegration, and many more energy losses."[**?**] This could be written in a short sense, that is, considering all losing and breaking factors of a cosmic ray particle.

Four primaries are considered, proton, helium, nitrogen, and iron, which are then mixed to generate mixed spectra from which the anisotrophy can be studied. The histogram on which the results are plotted is following Generalized Gumble function, which can be seen in Equation:6, which has its μ, σ , λ values hard code and it is following the EPOS-LHC model. [**?**] [**?**]

$$G(z) = \frac{1}{\sigma}\frac{\lambda^{\lambda}}{\Gamma(\lambda)}(e^{-\lambda z - \lambda e^{-z}}), \quad z = \frac{x-\mu}{\sigma} \tag{6}$$

The following provisional results can be see in the following Figures: 17 (**a**) and (**b**) for proton and iron, and Figure: 17 (**c**) and (**d**) for helium and nitrogen. It was intentionally plotted in such way that the differences between the lightest

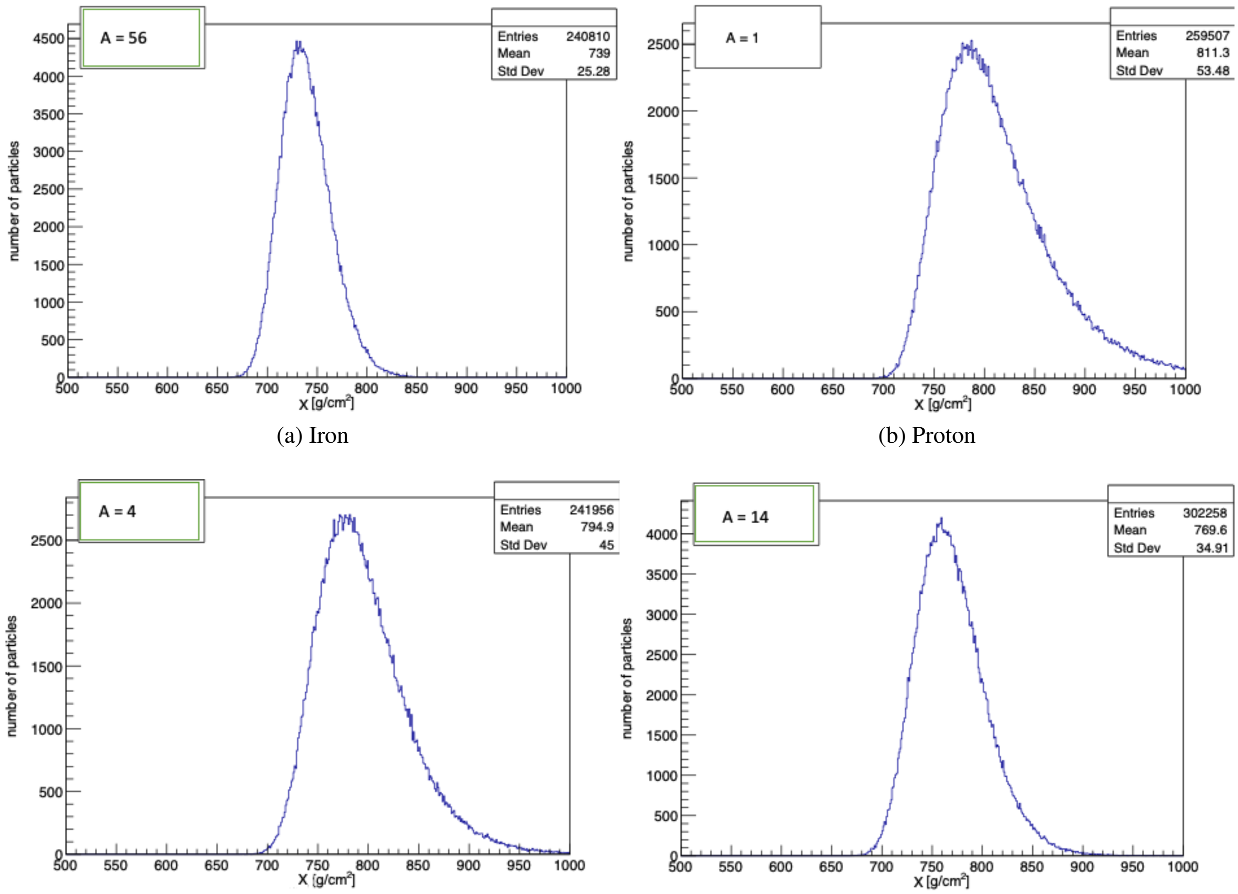

(a) Iron

(b) Proton

(c) Helium

(d) Nitrogen

Figure 17: Preliminary results of 4 primaries

and heaviest elements can be seen. Some interesting observations can be pointed out, such as the iron Xmax plot is more concentrated in the middle and does not spread too much where as the proton plot tends to spear more causing their mean values to be $(739 \pm 25.28)\ \mathrm{g/cm^2}$ and $(811.3 \pm 53.48)\ \mathrm{g/cm^2}$ for iron and proton respectively, this can also be seen in the case of helium and nitrogen with values of $(794 \pm 45.00)\ \mathrm{g/cm^2}$ and $(769 \pm 34.91)\ \mathrm{g/cm^2}$ respectively.

For now, the mixing part is only 50/50 ratio mixing of two primaries, the mixing of all primaries is still an ongoing project, however, even with the mix of only 2 primaries and interesting results can be observed, see Figure: 18 (**a**) for proton-iron mix , and (**b**) iron-nitrogen. Then Figure: 18 (**c**) proton-helium mix, and (**d**) proton-nitrogen. I exclude the results for helium-iron and helium-nitrogen as they are behaving in the same way as the already displayed light and heavy particle mixes.

Note that when these data will be compared to Auger observed data, an additional smearing of 20 g/cm^2 needs to be applied, otherwise the detector effects are not accounted for.

It is visible that the Xmax is indeed acting differently according to the particle, when there is 50/50 ratio mixing is taking some specific features from each of the components that are in the mix. Right now there is not much else to discover or to talk. The mixing of all 4 elementary particles is the essential step that will allow us to further dive into the anisotrophy and what ratio mixes are causing the anisotrophy and so on.

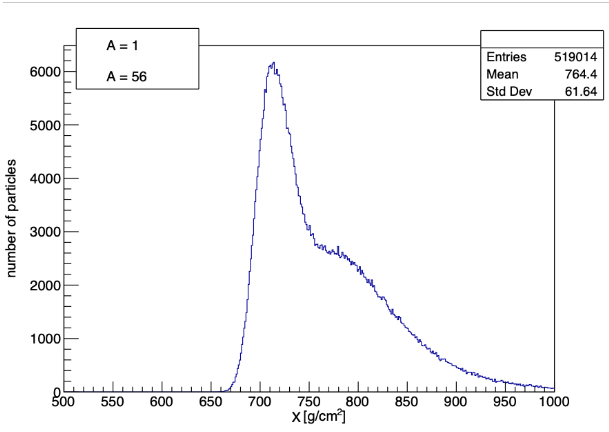

(a) Proton-Iron

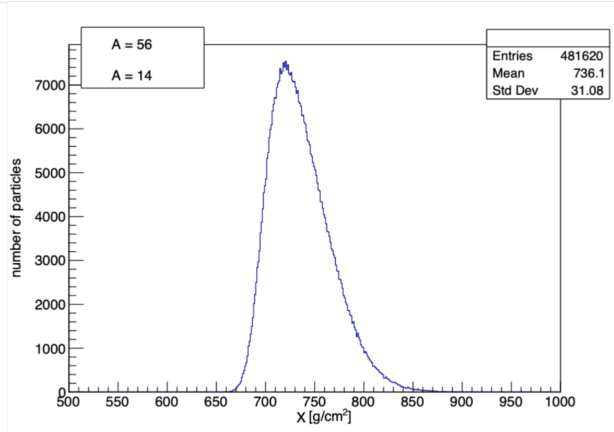

(b) Iron-Nitrogen

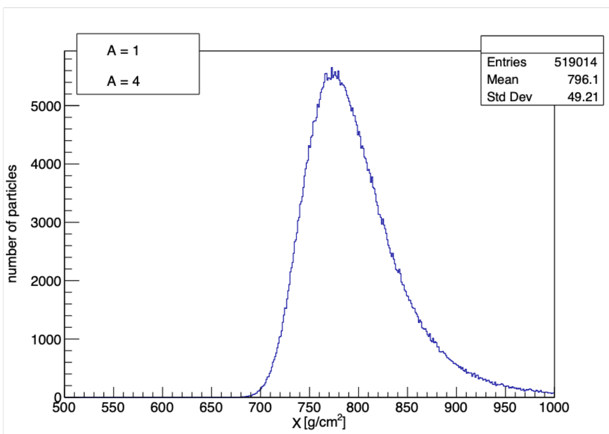

(c) Proton-Helium

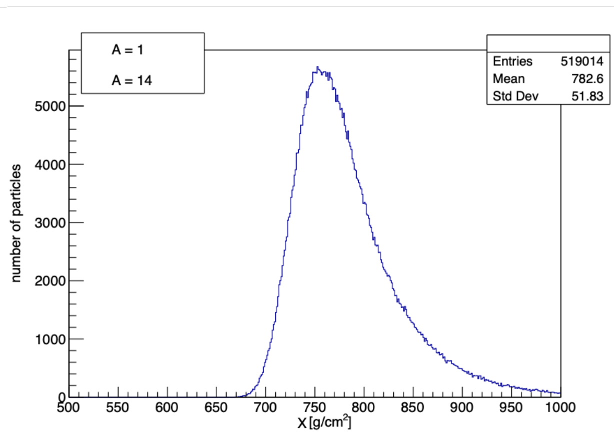

(d) Proton-Nitrogen

Figure 18: Preliminary results of 50/50 mixing

References

[1] L Adamczyk, J Kevin Adkins, G Agakishiev, MM Aggarwal, Z Ahammed, NN Ajitanand, I Alekseev, DM Anderson, R Aoyama, A Aparin, et al. Elliptic flow of electrons from heavy-flavor hadron decays in Au+Au collisions at $\sqrt{s_{NN}} = 200$, 62.4, and 39 GeV. *Physical Review C*, 95(3):034907, 2017.

[2] Xin Dong and Vincenzo Greco. Heavy quark production and properties of quark-gluon plasma. *Progress in Particle and Nuclear Physics*, 104:97–141, 2019.

[3] Xin Dong, Yen-Jie Lee, and Ralf Rapp. Open heavy-flavor production in heavy-ion collisions. *Annual Review of Nuclear and Particle Science*, 69:417–445, 2019.

[4] Mustafa Mustafa. Experimental study of electrons from heavy flavor hadrons decays in Au+Au collisions at 200, 62.4 and 39 GeV in the STAR experiment at RHIC. *PhD. Thesis. Purdue University*, 2013.

[5] KH Ackermann, N Adams, C Adler, Z Ahammed, S Ahmad, C Allgower, J Amonett, J Amsbaugh, BD Anderson, M Anderson, et al. STAR detector overview. *Nuclear Instruments and Methods in Physics Research Section A: Accelerators, Spectrometers, Detectors and Associated Equipment*, 499(2-3):624–632, 2003.

[6] Yi Yang. The STAR detector upgrades for the BES-II and beyond physics program. In *Quark Matter 2019*, 2019.

CONSTRUCTION AND COMISSIONING OF THE FDD DETECTOR

Vojtěch Zabloudil

1 Introduction

The ALICE (A Large Ion Collider Experiment) detector is undergoing a major upgrade of its setup throughout the Long Shutdown 2. The main difference for the upcoming Run 3 is the increase of the interaction rate to $50\,\mathrm{kHz}$ in Pb-Pb collisions and to $1\,\mathrm{MHz}$ in pp collisions, which is two orders of magnitude larger compared to Run 2. This demands improvements in data acquisition and computing infrastructure. The majority of the detectors switches to continuous readout, yet some of the older systems need an external trigger. In order to provide this task, while fulfilling the upgrade expectations, the new Fast Interaction Trigger (FIT) is added to the system.

The Fast Interaction Trigger is a system of three detectors: FT0, FV0 and Forward Diffractive Detector (FDD). The construction and installation of the latter is discussed in detail.

2 Forward Diffractive Detector

The FDD is a scintillation detector covering the forward pseudorapidity. It is divided into two stations: FDD-A and FDD-C which are located at a distance of $17\,\mathrm{m}$ and $19.5\,\mathrm{m}$ from the interaction point, respectively. The pseudorapidity coverage is from 4.8 to 6.3 for the FDD-A and from -7.0 to -4.9 for the FDD-C. Each station is made of two layers of plastic scintillators further subdivided into four quadrants. For each quadrant, there is a plastic scintillator connected to a pair of wavelength-shifting (WLS) bars that collect the light produced by the scintillator. The light is further transferred via optical fibres to a photomultiplier tube (PMT), where it is converted into the corresponding electrical signal.

3 FDD construction

The construction of the FDD is divided into several steps. Firstly, the WLS bars are glued to the scintillator, which together form a pad. The pad is then covered into aluminium foil in order to avoid external light coming into the pad. After two reflective layers, a layer for protective purposes is used. This consists of aluminium plates which provide protection against damage.

To complete the FDD module, the pads need to be connected to the PMTs by optical fibres. These are bunches of 96 optical fibres. The endings of the fibre bunches are glued together to properly fit the corresponding areas. A circular ending is on the PMT side, since the photocathode of the PMT is circular. The WLS bars are rectangular, so the fibres are shaped into a rectangle on this side.

4 Characterisation of the FDD photomultiplier tubes

The FDD funcionality heavily relies on the properties and quality of the used PMTs. For this purpose, twenty Hamamatsu H8409-70 fine-mesh PMTs were tested to choose the sixteen best-performing PMTs for the installation. This was done by irradiation of the PMTs with a low-intensity laser to get the single photon calibration. Two PMTs were used in one run, one whose voltage was set at different values to perform the calibration and the other operated at a constant voltage for reference purposes. The selection was done according to the relative amplitude and charge gain.

5 Installation of the FDD

The installation of FDD-C was carried out succesfully in February 2021, while the installation of FDD-A is planned for July 2021. When both stations are installed, the detectors will be connected to the electronics and subsequently tested in order to be ready to participate in pilot proton-proton collisions in October 2021.

Study of quarkonium production

Emanuel Bezányi

1 Introduction

Quarkonium studies play crucial role in determining the properties of the quark-gluon plasma. This hot and dense medium can be created in collisions of relativistic heavy nuclei. At high enough temperature in QGP, the Quarkonium states are suppressed due to Debye-like screening of $Q\bar{Q}$ potential. Although the QGP is not expected in proton-proton collisions, they provide a baseline for quarkonium production. The main variable of the observation is the nuclear modicfication factor R_{AA}, which quantifies the suppression by measuring the ratio of the quarkonium production of heavy-ion collisions to the production rate in collisions where QGP is not formed scaled by the average number of binary collisions.

2 Quarkonium production

Heavy quarks Q and antiquarks $\bar{Q}$ are created in the early stages of the collision. They can create bound states of quarkonium which are called charmonium for $c\bar{c}$ pair and bottomonium for $b\bar{b}$ pair. Measurements of quarkonium production in proton-proton collisions allow to test various production models which describe the formation of such bound states. The simplest quarkonium production model is the Color Evaporation Model, where the heavy quark pair neutralizes its color by interacting with the collision induced color field. The other main production models are the Color Singlet Model where the $Q\bar{Q}$ is produced directly in a colorless state and the Color Octet Model where the heavy quark pair is produced in an octet state and an additional gluon emission is needed to neutralize the color charge.

Quark-gluon plasma can be created in heavy ion collisions, if a sufficient temperature is reached. It is a state of matter, where quarks and gluons, which have to be bound under normal conditions, can move freely. Suppression of quarkonium production is expected in QGP because of the Debye-like color screening mechanism [2] and which can be expressed as $R_{AA} < 1$. Heavy quarkonium decays into hadrons in most of the cases but the small percentage decays into well observable leptons which do not interact strongly and therefore one can relatively easy detect and classify them. This was used also in our measurements.

3 STAR

The data recorded by STAR experiment at RHIC [4] are analyzed. This experiment focuses on heavy-ion collisions and to the study of the QGP and it consists of many detector subsystems. The Time Projection Chamber identifies charged particles and measures their momenta via energy loss. The Time of Flight measures the time of flight and with the knowledge of the path length of a particle we can determine its velocity. The Barrel Electromagnetic Calorimeter measures energy and it is used both for electron identification and as a high energy electron trigger. The Beam-beam counter is also used as a trigger.

4 Bottomonium measurements in the STAR experiment

Here we present, the recent results of bottomonium production studies measured by the STAR experiment. The experimental data from a proton-proton collision at $\sqrt{s} = 500$ GeV at STAR was compared with two production models

Figure 19, where the Color Evaporation model described them reasonably and the NRQCD with CGC overestimated the Υ production at low p_T. A gold-gold R_{AA} vs. collision centrality at $\sqrt{s_{NN}} = 200$ GeV was compared with Rapp's model [3] which includes regeneration and cold nuclear matter effects. This model describes data except for $\Upsilon(1S)$ in mid-central collisions.

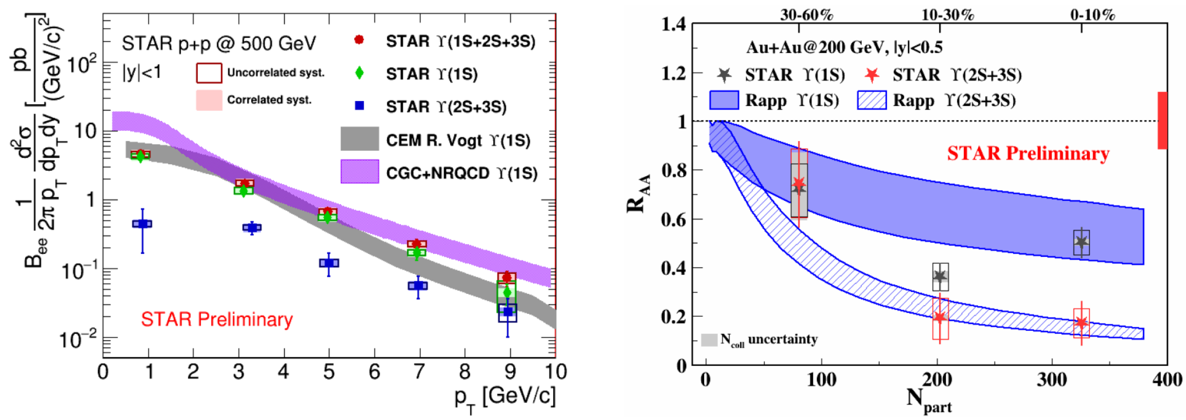

(a) Invariant cross section for inclusive Υ vs. p_T data compared with production models in proton-proton collision.

(b) Υ production in combined dielectron and dimuon channels in heavy-ion collision compared with Rapp's model calculation.

Figure 19: Bottomonium results for proton-proton and heavy-ion collisions. [1]

5 Data analysis

The main focus of this study is the proton-proton collision at $\sqrt{s} = 510$ GeV from 2017. A code was developed that focuses on the identification of high energy electrons with invariant mass greater than the mass of the Υ. It selected events, which contained a high energy electron. Good quality tracks were selected, identified as electrons using dE/dx and Barrel Electromagnetic Calorimeter information and combined into pairs for Υ signal reconstruction. Although some information was not yet available in our main dataset the code was tested on a gold-gold collision at $\sqrt{s_{NN}} = 54$ GeV recorded during the same year of running where the needed information is accessible. The code was tested on a small part of the data and the invariant mass was set to also look for J/ψ not only Υ. In the next step, the complete dataset will be analyzed and the obtained data evaluated.

References

[1] Leszek Kosarzewski. Overview of Upsilon production studies performed with the STAR experiment In *ICHEP2020* , 2021, 545.

[2] Tetsuo Matsui, Helmut Satz. J/ψ Suppression by Quark-Gluon Plasma Formation. In *Physics Letters B* 178, 1986, 416-422. ISSN 03702693.

[3] Xiaojian Du, Min He and Ralf Rapp. Color Screening and Regeneration of Bottomonia in High-Energy Heavy-Ion Collisions. In *Physical Review C* 96, 2017, 054901. ISSN 2469-9985.

[4] K.H. Ackermann et al. STAR detector overview. In *Nuclear Instruments and Methods in Physics Research Section A: Accelerators, Spectrometers, Detectors and Associated Equipment* 499, 2003, 624-632.

Application of relativistic fluid dynamics for the description of heavy ion collisions

Tomas Polednicek

1 Introduction

Heavy ion collisions allow us to create and study matter, which existed several microseconds after the Big Bang. This exotic fluid is called quark-gluon plasma (QGP) and is one of the main areas of research in particle physics.

The development of hydrodynamic descriptions of heavy ion collisions in recent years has shown its power and simplicity. The hydrodynamic approach makes it possible to simulate and understand the dynamics of a nuclear reaction in terms of macroscopic quantities such as energy density, temperature or pressure. It also creates a direct link to the equations of state and thus allows you to directly study how a particular equation of state affects observable quantities. In this work we focus on the description of heavy ion collisions and on the application of relativistic fluid dynamics in particle physics.

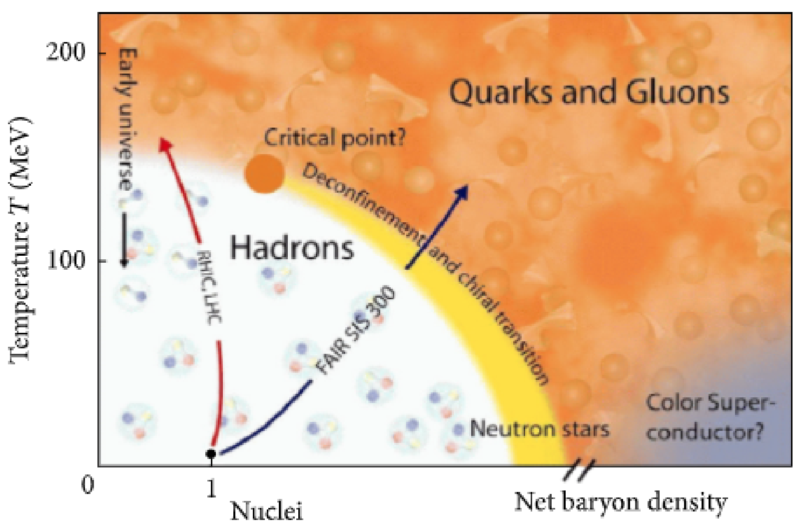

Figure 20: Schematic phase diagram of strongly interacting matter. [6]

2 Heavy Ion collisions

The main idea of a heavy ion physics is the description of hot and dense matter, which has an energy density much higher than $\epsilon_0 \simeq 0.15 \mathrm{GeV}/\mathrm{fm}^3$. At high energies or high temperatures, we expect that quarks (elementary building blocks of hadrons) become almost unbounded, so they can move freely. The quarks produced during the collision are concentrated in such a small volume. They can move almost freely and collective phenomena apply at the level of strong interactions. The theory describing this interaction is quantum chromodynamics (QCD). The residual interaction beyond the proton and neutron boundaries is then responsible for the bond between the nucleons in the nucleus.

Between the largest research centers, which deals with relativistic collisions of heavy ions, are included the BNL (Brookhaven National Laboratory) located in the United States and CERN (European Organization for Nuclear Research in 1986. Heavy ion collisions are currently being performed on RHIC (Relativistic Heavy Ion Collider) and LHC (Large Hadron Collider) accelerators, as well as the HADES experiment at GSI Darmstadt.

3 Relativistic hydrodynamics

Relativistic hydrodynamics is very interesting because it is simple and general. Simplicity is that the information about the system is encoded in its thermodynamic properties of the equation of state. Hydrodynamics is also general in the sense that it is based on only one assumption that we can neglect microscopic length scales against the length scale of the whole system. Another assumption regarding the nature of particles and their interactions, classical / quantum phenomena, is not made. In this simplicity lies the applicability of the hydrodynamic description in heavy ion collisions. We are able to describe the evolving system in covariant shape. The relativistic Euler equation (8), which describes motion of ideal fluid, can be easily determined as well as relativistic Navier-Stokes equation, which contains some correction, e.g. shear and bulk viscosity.

$$D\epsilon + (\epsilon + p)\nabla^{\perp}_{\mu} u^{\mu} = 0, \tag{7}$$

$$(\epsilon + p)Du^{\alpha} + \nabla^{\alpha}_{\perp} p = 0, \tag{8}$$

where ϵ energi density, p pressure, u^{μ} 4-velocity, $D \equiv u^{\mu}\nabla_{\mu}$ and $\nabla^{\alpha}_{\perp} \equiv \Delta^{\mu\alpha}\nabla_{\mu}$.

$$\begin{aligned} &D\epsilon + (\epsilon + P)\left(\nabla^{\perp}_{\lambda} u^{\lambda}\right) = \frac{\eta}{2}\sigma^{\mu\nu}\sigma_{\mu\nu} + \zeta\left(\nabla^{\perp}_{\lambda} u^{\lambda}\right)^{2}, \\ &(\epsilon + P)Du^{\alpha} + c_s^2 \nabla^{\alpha}_{\perp}\epsilon = \Delta^{\alpha}_{\nu}\nabla_{\mu}\left(\eta\sigma^{\mu\nu} + \zeta\delta^{\mu\nu}\left(\nabla^{\perp}_{\lambda} u^{\lambda}\right)\right), \end{aligned} \tag{9}$$

where ηresp. ζ, are shear resp. bulk viscosity coefficients and $\sigma^{\mu\nu} = 2\nabla^{(\mu}_{\perp} u^{\nu)} - \frac{2}{3}\Delta^{\mu\nu}\nabla^{\perp}_{\lambda} u^{\lambda}$. All these equations corresponds with their non-relativistic equivalent.

4 Hydrodynamic modeling in heavy ion physics

Hydrodynamic modeling of heavy ion collisions is performed in three stages. Three different models are used for the initial state (IS): UrQMD, GLISSANDO 2 or TRENTo. For all cases, the transition from the initial state to the dynamic description of fluid evolution or hydronynamization takes place at $\tau = \tau_0 = 1$. The subsequent hydrodynamic development of the hot and dense mass is performed using the 3 dimensional viscous code vHLLE. The transition from hydrodynamic expansion to particles takes place on the surface with a fixed energy of density $s_w = 0.5$ GeV/fm^3. When propagating to particles, the particles are sampled by phase space distributions using the Cooper-Fry formula, extended by shear viscosity corrections.

References

[1] J.D. Bjorken: Highly relativistic nucleus-nucleus collisions: The central rapidity region. Physical Review D 27 (1983) 140-151.

[2] P. Romatschke, U. Romatschke: Relativistic fluid dynamics in and out of equilibrium Cambridge UP, 2018

[3] P.F. Kolb, J. Sollfrank, U. Heinz: Anisotropic transverse flow and the quark hadron phase transition, Physical Review C62 (2000) 054909

[4] Iu. Karpenko, P. Huovinen, M. Bleicher: A 3+1 dimensional viscous hydrodynamic code for relativistic heavy ion collisions, Comput. Phys. Commun 185 (2014) 3016-3027

[5] Iu. Karpenko, P. Huovinen, H. Petersen, M. Bleicher: Estimation of the shear viscosity at finite net-baryon density from A+A collision data at $\sqrt(s_N N) = 7.7 - 200 GeV$, Physical Review 91 (2015) 064901

[6] P. Bicudo, PoS **FACESQCD** (2010), 015 doi:10.22323/1.117.0015 [arXiv:1102.5531 [hep-lat]].

Study of Upsilon meson production in the STAR experiment

Jakub Češka

1 Introduction

The main aim of the research in this proceeding is the study of Υ meson production in $\sqrt{s}$ = 510 GeV proton-proton collisions in the STAR experiment. Special emphasis of this work is the measurement of normalised Υ meson yield with regards to self-normalised event multiplicity. The Υ mesons are detected via the dielectron channel.

1.1 Quarkonia

The Υ meson is a part of the bottomonium family of particles, which are classified as quarkonia - a bound state of a heavy quark and its corresponding antiquark. The production mechanism of quarkonium is not yet well understood. Several quarkonium production models are in use today:

- colour singlet model, [1]
- colour octet model, [2]
- colour evaporation model. [3]

Also, in proton-proton collisions, quarkonia may be produced in multiple parton interactions (MPIs).

1.2 Effects on quarkonia

During high energy collisions there are several effects, which influence quarkonia and thus their yield, particularly when quark-gluon plasma (QGP) is created. One major effect is dissociation in QGP at high T via Debeye-like colour screening, where states with lower binding energy dissociate at lower T. There is also feed-down effect from excited states and heavier quarkonia, where the decay of heavier states influences the yield of lighter states. Other effects also include regeneration, which is small for Υ at RHIC energies, as well as cold nuclear matter effects, among which are nuclear absorption, comover interactions and nuclear PDF effects.

1.3 Motivation

The main motivation of this study, the Υ meson, can help with explaining the quarkonium production mechanism with increased precision compared to previous results. With the measurement of Υ p and p_{T} spectra, more information regarding the production mechanisms can be found. The Υ states ratios may shine light on production mechanisms and comover interactions. Proton-proton collisions also have the benefit of being a small interacting systems, where a possible colour glass condensate influence has been suggested [4]. The main aim of the study, the normalised event multiplicity dependence of the normalised Υ yield can be used to find out more about the MPI influence on Υ production.

2 STAR experiment

The Solenoidal Tracker at RHIC (STAR) detector is an experiment at the Relativistic Heavy Ion Collider (RHIC) in Brookhaven National Laboratory (BNL). The detector is intended primarily for QGP study. It consists of many sub-detectors, of which several are essential for this study. Those are the Time Projection Chamber (TPC), used for tracking and particle identification, the Time of Flight (TOF), used for multiplicity measurement and the Barrel Electromagnetic Calorimeter (BEMC), used as a trigger, as well as for electron and positron identification.

3 Data analysis

3.1 Data

The data analysed in this study is from proton-proton collisions at $\sqrt{s}$ = 510 GeV recorded by the STAR detector in its 2017 run (Run17). The chosen trigger is the BHT2*BBCMB, which should provide high-energy events, which are suitable for Υ analysis. The integrated luminosity of the new dataset is $\mathcal{L} \sim$ 340 pb^{-1}, which is an improvement over the Run11 data with $\mathcal{L} \sim$ 21.5 pb^{-1}. For now, the Run17 data does not have the BEMC information available and it is being reconstructed, so alternative methods of electron selection are employed.

3.2 Methodology

The code for the data analysis contains multiple segments, which take care of rejection of bad data and subsequent extraction of the signal, as well as other variables, which are important in the interpretation of the results.

First such segment is event selection, where only the events triggered by the BHT2*BBCMB trigger are accepted, which selects events with high energy BEMC hits and thus high Υ production probability. It also rejects events with the z position of the primary vertex $|v_{\mathrm{z}}|$ < 40 cm, which ensures uniform acceptance for each event.

The next part of the code deals with track selection. Here only good quality tracks with high number of TPC hits are selected. The measure of event multiplicity in this study is called TofMult. Only high quality tracks matched to TOF detector signal are selected, in order to have a stable measure of multiplicity unaffected by pileup.

Electrons and positrons will be selected according to the information obtained BEMC detector. Since the information is not yet available, other criteria are chosen. Firs of all, the candidate must fulfil all of the criteria for track selection. Furthermore, dE/dx information from the TPC is used to identify electrons.

The final part of the code so far is the Υ candidate reconstruction. The candidates are reconstructed using a Lorentz 4-vector addition provided by the ROOT software package. Only the candidates, where one of the electrons has p_{T} > 3 GeV/c and the other p_{T} > 1 GeV/c are accepted. From those candidates, two invariant mass spectra are produced: the unlike-sign spectrum (Fig. 21) should include both the signal and background, and the like-sign spectrum should be a reasonable approximation of combinatorial background. The invariant mass of the reconstructed particle in collider experiments with relativistic particles is defined as

$$m_{\mathrm{ee}}^2 = (E_1 + E_2)^2 - (\vec{p_1} + \vec{p_2})^2$$

4 Results and conclusion

The signal reconstruction has been tested on a smaller subset of the dataset. This can be seen in (Fig. 21), where the unlike-sign pair invariant mass spectrum in shown. The code also includes the candidate storage in ROOT trees, which will help with the subsequent analysis.

Further work will include the analysis of the entire dataset with new and improved electron selection criteria, once the data is reconstructed with the missing BEMC data. After that, the Υ signal extraction and the analysis of the results can follow.

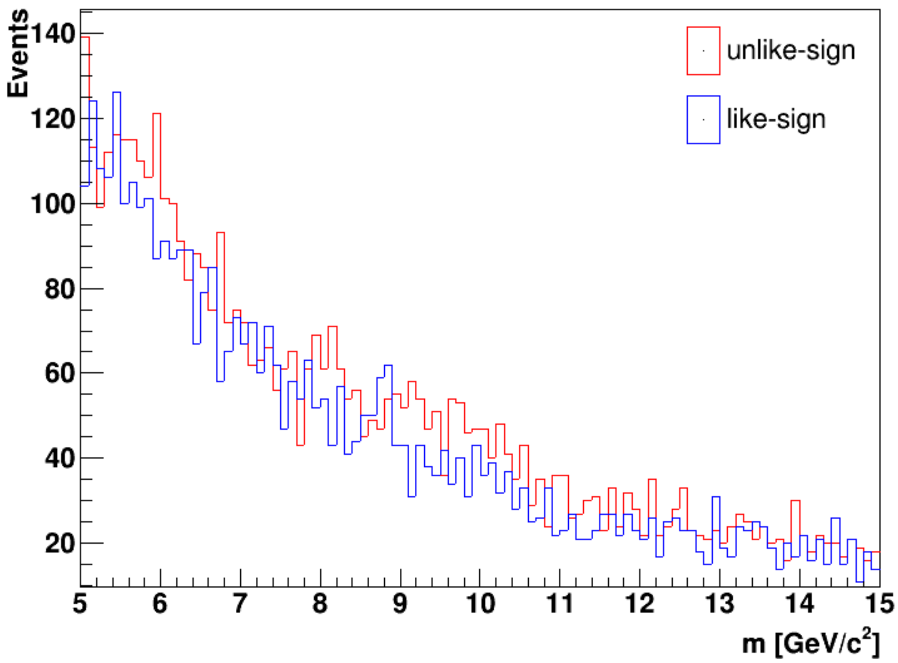

Figure 21: The invariant mass spectrum of unlike-sign pairs

References

[1] Chang Chao-Hsi. Hadronic production of J/Ψ associated with gluon. In *Nuc. Phys. B **172** (1980)*, pages 452–434.

[2] Geoffrey T. Bodwin *et al.* P-wave charmonium production in B-meson decays In *Phys. Rev. D **46** (1992)*, pages R3703–R3707.

[3] Harald Fritzsch Producing heavy quark flavors in hadronic collicions - A test of quantum chromodynamics In *Phys. Lett. B **67** (1977)*, pages 217-221

[4] E. G. Ferreiro and C. Pajares High multiplicity pp events and J/Ψ production at energies available at the CERN Large Hadron Collider In *Phys. Rev. C **86***, pages 034903

Reconstruction of longitudinal profiles of cosmic-ray showers using the shower geometry obtained from SD at Pierre Auger Observatory

Nikolas Denner

1 Introduction

The standard hybrid reconstruction of longitudinal profile at Pierre Auger Observatory uses signal in PMT pixels and arrival times from fluorescence telescopes together with arrival times on water Cherenkov station closest to the shower axis. Research conducted by my supervisors, Ing. Jakub Vícha, Ph.D. and Mgr. Vladimír Novotný, Ph.D. showed, that using not only the arrival times from surface detectors, but the whole SD geometry, is more precise for high quality SD data. This bigger precision yields $\sim$15% more events that pass through X_{max} cuts, which implies more statistics for high energy events. My task is to continue with this research and consider all of the changes and systematics in comparison with the standard reconstruction.

2 Longitudinal profile of cosmic-ray showers

The detection of cosmic-ray showers focuses mostly on the longitudinal profile reconstruction. That is because integral of longitudinal profile gives us the calorimetric energy of the shower. Full longitudinal energy deposit profile can be described by Gaisser-Hillas function [1]

$$f_{\text{GH}}(X) = \left(\frac{\mathrm{d}E}{\mathrm{d}X}\right)_{\text{max}} \left(\frac{X - X_0}{X_{\text{max}} - X_0}\right)^{\frac{X_{\text{max}} - X_0}{\lambda}} e^{\frac{X_{\text{max}} - X}{\lambda}}, \tag{10}$$

where $(\mathrm{d}E/\mathrm{d}X)_{\text{max}}$ is energy deposit at $X = X_{\text{max}}$, X_{max} is the depth of the shower maximum and X_0 and λ are shape parameters.

Slant depth X [g·cm^{-2}] can be understood as the amout of materials penetrated by the shower. It is given as integral of material density over path length. Parameters X_0 and λ are constrained to their average values.

In practice, photoelectrons detected in PMTs of fluorescence telescopes are fitted by equation (10). This fit is then integrated, which gives us energy deposited by the shower in the atmosphere. Finally, the total energy is estimated by correcting this for energy carried away by neutrinos and undetected muons.

3 The Pierre Auger Observatory

3.1 Detection of cosmic-ray showers

The Pierre Auger Observatory uses hybrid approach to cosmic-ray shower detection. This approach consists of two parts, a surface detector (SD), which is composed of 1660 water Cherenkov stations, and a fluorescence detector (FD), composed of 27 fluorescence telescopes [1].

The water Cherenkov stations are distributed over an area of $\sim$3000 km^2 and each station is 1.5 km away from the others. There is also a small array of these stations, where the spacing between them is only 750 m. These stations operate nearly 100% of the time.

Fluorescence telescopes are stationed in four locations and overlook the SD array. These telescopes operate only about 13% of the time due to their sensitivity. This estimated duty cycle is given by their need for moonless nights in combination with favorable meteorological conditions.

3.2 Shower reconstruction

The reconstrucion of events in the Pierre Auger Observatory works in the following way. First, the signal from PMT pixels of the FD is used to reconstruct the shower axis plane. Then, 3D reconstruction of axis direction is obtained from arrival times of light on FD and from arrival times on SD station closest to the shower axis. This is the so-called hybrid reconstruction of events.

Reconstruction of events with the help of SD geometry would use not only the arrival times on the SD station closest to the shower axis, but also the strenght of the signal in various stations. This approach is more precise for high quality SD data because the hybrid reconstruction sometimes miscalculates the shower axis position. This type of reconstruction yields about 15% more event that pass through X_{max} cuts and can therefore be used for further research.

3.3 Auger Offline

Reconstruction of events is performed within the Pierre Auger Observatory offline software framework, also called Auger Offline. This framework introduces infrastructure which supports a variety of distinct computational tasks that are necessary for analyzation of gathered data [2]. Auger Offline can be divided into three main parts: processing modules, event data model and detector description.

Modules are codes used for various processing of data. They are sequenced together using instructions from XML file. Auger Offline allows all its users to look into these codes and use them in desired way. Event data model is used to accumulate all simulation and reconstruction information. And finally detector description provides configuration and performance data of the observatory and also atmospheric conditions as a function of time.

References

[1] A. Aab et al. [Pierre Auger Collaboration], Phys. Rev. D **90** (2014) no.12, 122005 doi:10.1103/PhysRevD.90.122005 [arXiv:1409.4809 [astro-ph.HE]]doi:10.1109/NSSMIC.2004.1462607

[2] S. Argiro, L. Nellen, T. C. Paul, T. Porter and L. Prado, Jr., doi:10.1109/NSSMIC.2004.1462607

THE EVOLUTION OF MOMENTUM ANISOTROPIES IN HEAVY-ION COLLISIONS

Bc. Tomáš Novák

1 Quark-gluon plasma in heavy ion collisions

We study the formation and evolution of quark-gluon plasma (QGP) in high energy collisions of heavy ions. In sufficient energies two nucleuses pass each accompied with collision of its nucleons and polarization of vacuum, which later produces high amount of hadronic matter. We focus on deposited energy in mid-rapidity region in transversal plane of non-central collision in 30-40 % centrality. Typical eliptic profile of deposited energy can be seen on a Fig. 22 - **Left**. There are evidences of the collective behaviour of QGP namely *anisotropic angular distribution of detected hadrons* $dN/dyd\phi dp_T$ which prefers high *elliptic flow coefficient* v_2 defined as:

$$\frac{\mathrm{d}N}{\mathrm{d}y\mathrm{d}\phi\mathrm{d}p_T} = \frac{\mathrm{d}N}{\mathrm{d}y\mathrm{d}p_T}\Big(1 + 2v_1(p_T)\cos[\phi-\Psi_1] + 2v_2(p_T)\cos[2(\phi-\Psi_2)] + \dots\Big),$$

$$\text{where } v_n = \frac{\int \mathrm{d}\phi \cos[n(\phi-\Psi_n)]\frac{\mathrm{d}N}{\mathrm{d}y\mathrm{d}\phi\mathrm{d}p_T}}{\int \mathrm{d}\phi\frac{\mathrm{d}N}{\mathrm{d}y\mathrm{d}\phi\mathrm{d}p_T}}$$

$$\text{and } \Psi_n = \frac{1}{n}\arctan\frac{\langle p_T \sin n\phi\rangle}{\langle p_T \cos n\phi\rangle}, \; p_T = \sqrt{p_x^2+p_y^2}.$$

Propagation of initial elliptic energy density profile into elliptic flow v_2 is interpreted as result of anisotropic expansion driven by gradients in pressure. From the initial elliptic profile the pressure gradient is highest in the direction of minor axis of ellipsis, and so it determines the flow of matter as we see as arrows on Fig. 22 - **Right**.

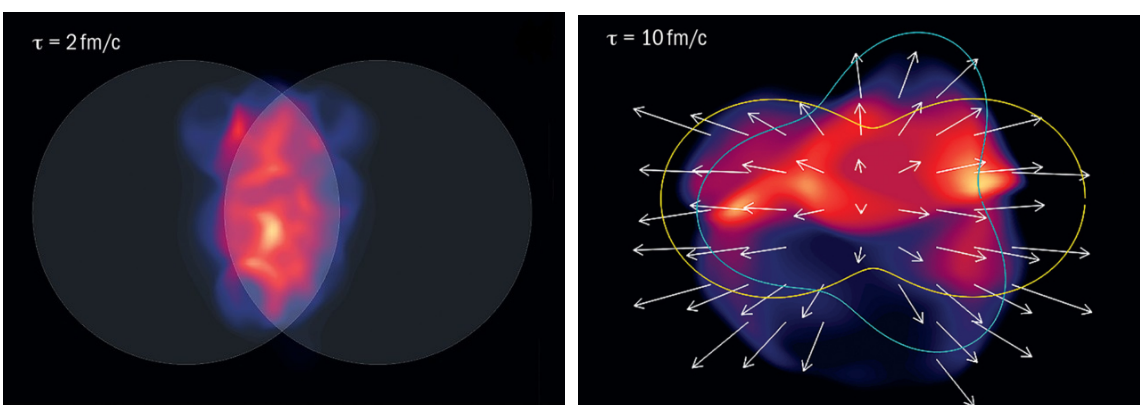

Figure 22: **Left:** Typical elliptic profile of initial energy density. **Right:** Evolution of elliptic profile into anisotropic flow, flow is highlighted by arrows. 7

2 Relativistic hydrodynamics

Flow of matter driven by gradients in pressure is typical for fluids, therefore the *relativistic hydrodynamics* as the suited macroscopic fenomenological theory of QGP was intorduced. There we forming the equations of motion for fluids in high energy scales, which in limit case of low energies corresponds to classical hydrodynamical equations of motion. Relativistic description depends on explicit form of *energy momentum tensor* $T^{\mu\nu}$ as the equations of motion are obtained from covariant conservation of selected energy momentum tensor:

$$\nabla_\mu T^{\mu\nu} = 0. \tag{11}$$

We also have additional evolution equations to (11), which corresponds to the coservation laws of conserved charges (baryon number). Our phase variables are velocity field u^μ, scalar field – energy density ε, pressure p and others. For zeroth order energy momentum tensor $T^{\mu\nu}_{(0)}$ we may choose explicit form

$$T^{\mu\nu}_{(0)} = \epsilon u^\mu u^\nu + p\Delta^{\mu\nu} \tag{12}$$

which is implemented in utilized hydrodynamic code `vHLLE`.

3 Implementing spatial and momentum anisotropies into vHLLE

For simulating of initial state we have choosed code `GLISSANDO 2` [4], which output is suitable for further hydrodynamic evolution in `vHLLE` [6]. In event by event simulations we study *spatial* and *momentum anisotropies*, which are implemented into `vHLLE`. Anisotropies quantify difference in evolution of QGP in transversal plane from the situation of isotropic central collision with circular energy density profile. Spatial anisotropies are defined as

$$\epsilon^x_{m,n}(\tau) = -\frac{\int dxdy\ \varepsilon(x,y,\tau) r^m \cos[n(\phi - \Psi_{m,n})]}{\int dxdy\ \varepsilon(x,y,\tau) r^m}, \tag{13}$$

where phase is defined from initial energy density profile $\varepsilon(x, y, \tau_0)$:

$$\Psi_{m,n} = \frac{1}{n} \arctan \frac{\int dxdy\ \varepsilon(x,y,\tau_0) r^m \sin[n\phi]}{\int dxdy\ \varepsilon(x,y,\tau_0) r^m \cos[n\phi]} + \frac{\pi}{n}. \tag{14}$$

We have defined new variables in orders n and m and in same style we may introduce momentum anisotropies:

$$\epsilon^p_{m,n}(\tau) = \frac{\int dxdy\ \sqrt{(T^{01})^2 + (T^{02})^2} r^m \cos[n(\phi - \Psi_{m,n})]}{\int dxdy\ r^m T^{00}}. \tag{15}$$

Those new variables characterize evolution of QGP in transversal plane in spatial and momentum domain. Therefore it is natural to present conjecture about relation of anisotropies $\epsilon^x_{m,n}(\tau), \epsilon^p_{m,n}(\tau)$ in all orders m, n and phase variables – fields $u^\mu(\boldsymbol{x},\tau), \varepsilon(\boldsymbol{x},\tau), p(\boldsymbol{x},\tau), \ldots$. The conjecture is following:

> In hydrodynamical simulations inifinite dymensional hydrodynamical system is discretized, so we obtaine state vector $\xi(\tau)$. If we consider infinitely many spatial and momentum anisotropies $\epsilon^x_{m,n}(\tau), \epsilon^p_{m,n}(\tau)$ in orders m, n we may reconstruct fields $u^\mu(\boldsymbol{x},\tau), \varepsilon(\boldsymbol{x},\tau), p(\boldsymbol{x},\tau), \ldots$. As if anisotropies are another variable system, then the state vector $\xi(\tau)$ could be explicitly function of anisotropies:
>
> $$\boldsymbol{\xi}(\tau_j) = \left(\epsilon^x_{1,1}, \epsilon^p_{1,1}, \epsilon^x_{1,2}, \epsilon^p_{1,2}, \ldots\right)^{\mathrm{T}}. \tag{16}$$
>
> We may project this vector onto lower dimensional space by some measurement functions $\eta_i = \eta_i(\epsilon^x_{m,n}, \epsilon^p_{m,n})$:
>
> $$\tilde{\xi}(\tau_j) = \left(\eta_1(\epsilon^x_{m,n}, \epsilon^p_{m,n}), \eta_2(\epsilon^x_{m,n}, \epsilon^p_{m,n}) \ldots, \eta_h(\epsilon^x_{m,n}, \epsilon^p_{m,n})\right)^{\mathrm{T}}, \tag{17}$$
>
> this projection of state vector could be further studied.

4 Event by event analysis

Further we have fixed $m = 2$ for all anisotropies. In results we have clearly seen proportionality of maximum momentum anisotropy $\bar{\epsilon}^p_n \equiv \max_\tau |\epsilon^p_n(\tau)|$ to the initial value of spatial anisotropy $\bar{\epsilon}^x_n \equiv= \epsilon^x_n(\tau_0)$ in the same orders n. On Fig. 23 - **Left** we see dynamical correlation of sums $\bar{\epsilon}^p_2 + \bar{\epsilon}^p_3 + \bar{\epsilon}^p_4$ and $\bar{\epsilon}^x_2 + \bar{\epsilon}^x_3 + \bar{\epsilon}^x_4$. To test the conjecture we build correlation of sums $\bar{\epsilon}^x_n + \bar{\epsilon}^p_n$ in three dimensions for $n = 2, 3, 4$ on Fig. 23 - **Right**. We may see the black curve – averaged evolution, which corresponds to the trend.

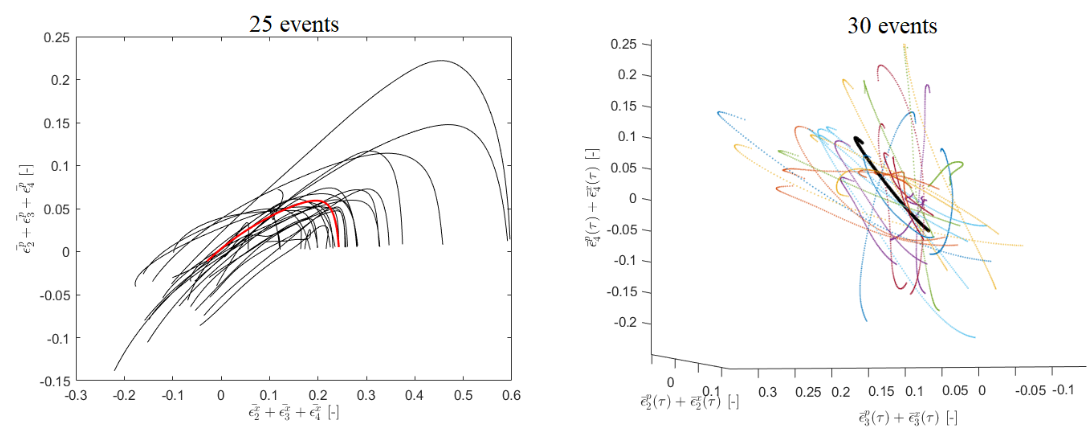

Figure 23: **Left:** Correlation of $\bar{\epsilon}^x_2(\tau) + \bar{\epsilon}^x_3(\tau) + \bar{\epsilon}^x_4(\tau)$ and $\bar{\epsilon}^p_2(\tau) + \bar{\epsilon}^p_3(\tau) + \bar{\epsilon}^p_4(\tau)$ with its average (red). **Right:** Correlation of $\bar{\epsilon}^x_2(\tau) + \bar{\epsilon}^p_2(\tau)$, $\bar{\epsilon}^x_3(\tau) + \bar{\epsilon}^p_3(\tau)$ and $\bar{\epsilon}^x_4(\tau) + \bar{\epsilon}^p_4(\tau)$ shown on axis x, y, z, also with averaged evolution (black).

References

[1] PASENCHNIK, R., M. ŠUMBERA *Phenomenological Review on Quark-Gluon Plasma: Concepts vs. Observation*. 2017. `arXiv:1611.01533v3`

[2] FLOECHINGER, S., U. A. WIEDEMANN *Kinetic freeze-out, particle spectra, and harmonic fow coefficients in mode by mode hydrodynamics*. 2014. Phys. Rev. C 89 (2014) 034914

[3] SONG, H., U. HEINZ *Multiplicity scaling in ideal and viscous hydrodynamics*. 2008. Phys. Rev. C 78 024902

[4] BRONIOWSKI, W., M. RYBCZYŃSKI, P. BOŻEK *GLISSANDO: GLauber Initial-State Simulation AND mOre... ?*. 2008. `arXiv:0710.05731v3`

[5] NEIMI, H. *Event-by-event distributions of azimuthal asymmetries in ultrarelativistic heavy-ion collisions*. 2013. Phys. Rev. C 87 054901

[6] KARPENKO, Iu., P. HUOVINEN, H. PETERSEN *A 3+1 dimensional viscous hydrodynamic code for relativistic heavy ion collisions*. 2014. Comput. Phys. Commun 185 3016-3027

[7] *Going with the flow*. Anisotropic expansion. `https://laptrinhx.com/news/going-with-the-flow-kZlDaDG/`